Miniaturized 3–D Mapping System Using a Fiber Optic Coupler as a Young's Double Pinhole Interferometer

Timothy L. Pennington, B.S.E.E., M.S.E.E.

Captain, USAF

Dissertation submitted to the Faculty of the

Virginia Polytechnic Institute and State University

in partial fulfillment of the requirements for the degree of

Doctor of Philosophy

in

Electrical Engineering

Anbo Wang, Chair

Richard Claus

Guy Indebetouw

Ahmad Safaai–Jazi

Russell May

5 June 2000

Blacksburg, Virginia

Keywords: Fiber Optics, Fiber Optic Coupler, Interferometer, 3–D Mapping, Young's Double Pinhole Interferometer.

Miniaturized 3–D Mapping System Using a Fiber Optic Coupler as a Young's Double Pinhole Interferometer

Timothy L. Pennington

(ABSTRACT)

Three–dimensional mapping has many applications including robot navigation, medical diagnosis and industrial inspection. However, many applications remain unfilled due to the large size and complex nature of typical 3–D mapping systems. The use of fiber optics allows the miniaturization and simplification of many optical systems. This research used a fiber optic coupler to project a fringe pattern onto an object to be profiled. The two outputs fibers of the coupler were brought close together to form the pinholes of a Young's Double Pinhole Interferometer. This provides the advantages of this simple interferometer without the disadvantage of power loss by the customary method of spatially filtering a collimated laser beam with a pair of pinholes. The shape of the object is determined by analyzing the fringe pattern. The system developed has a resolution of 0.1mm and a measurement error less than 1.5% of the object's depth. The use of fiber optics provides many advantages including: remote location of the laser source (which also means remote location of heat sources, a critical requirement for many applications); easy accommodation of several laser sources, including gas lasers and high–power, low–cost fiber pigtailed laser diodes; and variation of source wavelength without disturbing the pinholes. The principal advantages of this mapping system over existing methods are its small size, minimum number of critically aligned components, and remote location of the laser sources.

Disclaimer

The views expressed in this document are those of the author and do not reflect the official policy or position of the Air Force, the Department of Defense or the U. S. Government.

Dedication

This work is dedicated to my loving wife Amy, for her undying support, and to my wonderful daughter Sarah for her bright smiles.

Acknowledgments

There are many people who made this work possible. Most importantly, my wife, Amy, provided encouragement and support during the difficult times. She took care of so many other "details" so that I could concentrate on my research. Also, my daughter Sarah's nightly request to "come play" helped remind me that family is more important than any number of academic degrees. Further, it was the seeds of a Christian faith and work ethic, implanted by my parents, that caused me to perform well enough in my early years of school to make graduate study possible. Lastly, I greatly appreciate the technical advice and encouragement provided by Anbo Wang, Russell May, and Hai Xaio during this research.

Contents

1 Introduction **1**

2 Background **3**

2.1 Interferometry as a Profilometer 4

2.2 Interferogram Phase Detection 5

2.2.1 Phase–Shifting Interferometry 6

2.2.2 Fourier Transform Fringe Analysis 8

2.3 Phase Unwrapping 10

2.3.1 Unwrapping methods that accommodate step discontinuities 13

3 System Design and Manufacturing **15**

3.1 Mathematical Model of Fringe Projector 18

3.2 Phase Determination and Unwrapping 22

3.3 System Analysis 24

3.3.1 Optimum Viewing Angle 24

3.3.2 Fringe Generator Subsystem 25

3.3.3 Camera and Laser Subsystems 31

3.4 Manufacturing Process 33

3.4.1 Initial Attempt to Polish a Standard Coupler 34

3.4.2 Manufacturing of a 50/50 coupler at two wavelengths 43

3.4.3 Polishing Specialized Couple using White–Light–Interferometer . . . 44

3.4.4 Fiber Alignment and Calibration 49

4 Results and Discussion **52**

4.1 Reconstruction of a Doll's Face 52

4.2 Reconstruction of a Soda Can 55

4.3 Reconstruction of a Flat Plate and System Resolution 57

5 Conclusions **65**

A Detailed Analysis of Optimum Viewing Angle **68**

List of Figures

3.1 Top–level system description 16

3.2 Example of fringe pattern on a flat object and on a triangular object 17

3.3 Coordinate Systems 19

3.4 Example of Phase Computation. 23

3.5 Estimated System Resolution 26

3.6 Schematic of fiber alignment 29

3.7 Temperature sensitivity 30

3.8 Temperature sensitivity for insulated fibers 31

3.9 Laser power requirements 32

3.10 First attempt to manufacture Young's pinhole interferometer 34

3.11 Fringe Pattern and Coupler Endface images 36

3.12 Gaussian approximation to mode–field distribution 37

3.13 Intensity distribution from modeled coupler 38

3.14 Calculate fringe pattern, no wedge 40

3.15 Calculate fringe pattern, 5 degree wedge 41

3.16 Calculate fringe pattern, 5 degree wedge plus rotation 42

3.17 Coupler manufacturing station 43

3.18 White light interferometer 45

3.19 Polishing the specialized coupler 45

3.20 Initial white light interferometer spectrum 46

3.21 Mid-way white light interferometer spectrum 47

3.22 Initial and final white light interferometer spectrum 47

3.23 A low–pass filtered version of a spectra in Figure 3.22. 48

3.24 Fringe pattern after alignment 49

4.1 Picture of doll used as test object. 53

4.2 HeNe fringes on the doll's face. 53

4.3 Reconstructed surface of doll's face 54

4.4 Reconstructed surface of a soda can. 56

4.5 Comparison of reconstructed can surface to a cylinder. 57

4.6 Flat plate with 2mm step 58

4.7 Measured surface of flat plate with 2mm step 59

4.8 Cross–section of flat plate profile. 60

4.9 Representative raw fringe pattern 61

4.10 Correlation between zero order fringe and surface height 62

4.11 Correlation coefficient as a function of x_o. 63

A.1 Coordinate systems 70

A.2 Estimate system resolution 71

A.3 Camera pixel size 72

Chapter 1 Introduction

"A picture is worth a thousand words," or so the saying goes. That statement is still true even in today's computer world and can even be true *of computers.* One example is providing a computer a "picture" of a 3–D object for various reasons such as inspection, navigation, or process control. Enabling a computer to see in 3–D greatly enhances its ability to perform various tasks. Several methods exist to generate the 3–D representation or profile of an object. Many of these techniques require contact with the object, which is not possible in many situations. Over the past few decades, many non-contact profilometers have been developed for various applications [8]. Some of these profilometers are based on radar imaging, laser scanning, interferometry, contrived lightening, triangulation and Moire.

While all of these methods have their advantages, all of them are also either slow, or require large bulky optics and/or lightening conditions. Therefore, a need exists for a simple, compact, 3–D mapping system that can be used on a variety of platforms. The system developed during this research consists of a simpler design than the methods currently used. The heart of the system is a Young's Double Pinhole interferometer constructed from a simple two by two fiber optic coupler. The fringe pattern is projected onto the object and viewed with a camera. The shape of the object is determined from the fringe pattern.

While fringe projection is not a new technique [26], many applications use collimated fringes. This greatly simplifies the mathematics and allows the reconstruction of the object from the fringe pattern to proceed smoother. However, it also requires that the object be

no larger than the optics, *e.g.* if you need to generate the profile for a ten by ten inch engineering object, you will need optics on the order of twelve inches in size. Obviously, the system would become very bulky, heavy, and *expensive*. A system that uses a diverging fringe pattern would minimize the size and cost of the optics. The double pinhole interferometer satisfies that requirement.

Such a system has been developed in the course of this research. The system has an R.M.S. error of approximately 1.5% of the object's depth and a resolution of 0.1mm. For these results, the object was located about one–half meter away and the mapping area was approximately 55mm by 41mm.

Chapter 2 provides some further background and describes in greater detail the other methods of performing 3–D mapping. Chapter 3 describes the system design, the theory behind its operation, and the manufacturing and implementation of the system. An analysis of the major system parameters is also included. Chapter 4 shows some sample results and analyzes the system's resolution and measurement accuracy. Finally, Chapter 5 draws the conclusions.

Chapter 2 Background

Three–dimensional mapping of an object has long been in use and has gone by several names. Some of these names include 3–D mapping, topography [49], profilometry [26], depth mapping [31], range imaging [31], and a variety of others.

The methods of generating a surface map can be broken down into two categories, contact and non–contact measurements. Contact measurements are generally used for metallic objects and involves moving a probe along the surface of the object and measuring its deflection as a function of spatial coordinates. While this is a suitable method for many applications, such as measuring automobile parts or unpolished optics, it is entirely unacceptable for many others. A contact profilometer would not be allowed, for example, to measure the polished surface of the primary mirror on a meter-class telescope. Further, a contact profilometer can not be used when physical barriers prevent contact with the object. Thus, non–contact profilometers have been developed to meet these needs.

The methods of generating non–contact surface mapping are as varied as the applications. Airplanes use radar and coherent phase detection to determine the profile of the landscape below. Other applications use a single point source, scanned along the object, to determine the profile using the time of travel of the pulse from the source to the object and back to the detector [20, 27, 47, 64].

2.1 Interferometry as a Profilometer

For smaller and higher precision requirements, interferometry, or the interference of two coherent sources, has become the method of choice. Within seconds, interferometry can measure the profile of an object with a repeatability on the order of one-thousandth of a wavelength [12, 40]. As always, there is a trade off between precision and measurement range. For surface mapping of larger objects, a longer wavelength, or at least a longer *effective* wavelength is required. One method of extending the dynamic range is through the use of fringe projection. The effective wavelength is equal to the period of the fringes on the object. This allows the system to be designed to meet the measurement requirements of that particular application.

Several methods exist to project interference fringes onto the surface. Perhaps one of the most popular methods is through the use of a transparency [1] or a Ronchi grating [5, 9, 62, 70]. If the fringe pattern projected onto the object is viewed through the same, or a similar, grating, the Moire pattern will be visible allowing the measurement of nearly flat objects [28]. Another method of projecting fringes is by the interference of two coherent beams on the objects surface [61] or a holographic plate [33, 45]. A few researchers are taking advantage of some of the latest electro–optic technology and using a spatial light modulator to generate the fringes [39, 50, 55, 60]. This technique has the advantage that the phase or spacing of the fringes can be adjusted without any "moving parts," thus allowing easy adjustment of

[1] Even though "fringes" produced by the shadow of a transparency are not true interference fringes, referring to them as interferograms or interference fringes is justified in the context of this work since the image analysis procedures are the same [46].

the precision and measurement range.

2.2 Interferogram Phase Detection

Whatever the method of fringe generation, the task still remains to relate the location of the fringes to the surface profile. Before that step can be completed, however, the interferogram must be analyzed to determine the phase of the fringes at each location. Early methods of performing this task were intensity based [46, 49, 68, 72]. That is, the intensity of the interferogram is analyzed to trace the fringe maximum and/or minimum locations. Several digital image preprocessing techniques such as smoothing, thinning and skeletoning, were used to aid in this process. Once completed, the fringes had to be properly ordered before the phase could be determined. This proved to be one of the more challenging task in automating the fringe analysis.

In recent years, phase–measurement interferometry has become the preferred method of analyzing interferograms [11, 12, 46]. In this technique, the phase of the fringe pattern is determined directly through either a phase–stepping technique [4] or Fourier transform analysis [66]. The final operation in both methods involves an inverse tangent function. Hence the calculated phase map is a wrapped (modulo 2π) version of the true phase map. Some sort of "phase unwrapping" procedure must then be performed. This process will be discussed further in Section 2.3. Which method is used is largely application dependent. If the atmospheric and mechanical conditions are stable enough to allow the acquisition of

three or more phase–shifted interferograms, phase–shifting interferometry is the method of choice [58]. However, many applications exist in which there is not sufficient time to capture three or more interferograms before conditions change. In this circumstance, the Fourier transform method is used.

2.2.1 Phase–Shifting Interferometry

Phase–shifting interferometry involves capturing multiply phase shifted interferograms of the same object. The interferogram can be expressed as

$$I_i(x,y) = I_o(x,y)\left[1 + \gamma_o \cos(\phi + \alpha_i)\right], \qquad i = 1, \ldots, N. \tag{2.1}$$

where I_o is the dc intensity, γ_o is the fringe visibility and α_i is the phase shift corresponding to the i^{th} interferogram. If the phase shifts are chosen such that the N measurements are equally spaced over one modulation period, i.e.

$$\alpha_i = \frac{i2\pi}{N}, \qquad i = 1, \ldots, N, \tag{2.2}$$

then the phase of the interferogram at each point can be determined by [4, 12]

$$\phi(x,y) = \tan^{-1}\left[\frac{\sum I_i(x,y)\sin(\alpha_i)}{\sum I_i(x,y)\cos(\alpha_i)}\right]. \tag{2.3}$$

In equation 2.1, there are three unknowns, the dc intensity, the fringe visibility and the fringe phase. Hence we must capture at least three interferograms to solve for those variables. If we choose $\alpha_i = \pi/4, 3\pi/4,$ and $5\pi/4$, then the phase can be determined from

$$\phi = \tan^{-1}\left[\frac{I_3 - I_2}{I_1 - I_2}\right]. \tag{2.4}$$

Perhaps the most commonly used algorithm, however, is the four–frame method [2, 12, 23, 54, 73]. In this technique, four frames are captured with a $\pi/2$ phase shift between each frame. The phase is then obtained by

$$\phi = \tan^{-1}\left[\frac{I_4 - I_2}{I_1 - I_3}\right], \tag{2.5}$$

where,

$$I_i = I_o\left[1 + \gamma_o \cos\left(\phi + (i-1)\frac{\pi}{2}\right)\right]. \tag{2.6}$$

Recently, de Groot [13] has commented that the development of phase–shifting interferometry algorithms occurred during a time when computer memory was expensive and hence they were driven to use the least number of frames possible. However, in today's climate of falling computer memory and processor prices, those methods could be revamped. By looking at phase–shifting interferometry from the frequency domain perspective, de Groot suggested that much of the noise sensitivity could be improved by using non–rectangular sampling windows, such as the Von Hann window, also called the raised cosine. Using this

approach, he developed several algorithms using up to twelve phase–shifted interferogram frames.

Several methods exist for producing the phase shift. Some of the more common include mechanically translating a grating [37, 70], moving a mirror in the reference arm of a Michelson or Twyman–Green [4] interferometer, or varying the wavelength using a tunable laser diode [29].

2.2.2 Fourier Transform Fringe Analysis

An underlying requirement of phase–shifting interferometry (PSI) is that everything remains mechanically and optically stable during the time the phase is varied and the fringe patterns are captured. This requirement can not be met for many applications due to vibration, transient events, or atmospheric turbulence. Another difficulty with PSI is that the phase shift must be generated in some manner with high precision. This is usually done either by mechanically moving a mirror, or by some electro–optic device. This may not always be possible for measurements in harsh environments. Hence the phase determination of the fringe pattern must be performed with a single fringe pattern. In these applications, Fourier Transform methods [66, 67] are applicable.

If the reference mirror of an interferometer is tilted slightly, "carrier fringes" of a known

spatial frequency will develop. The fringe pattern can then be rewritten as:

$$g(x,y) = a(x,y) + b(x,y)\cos\left[2\pi f_o x + \phi(x,y)\right], \tag{2.7}$$

where $a(x,y)$ is the background, $b(x,y)$ represents unwanted irradiance variations due to nonuniform light reflection or transmission, f_o is the frequency of the carrier fringes and $\phi(x,y)$ is the desired phase information. Equation 2.7 can be rewritten in the form of

$$g(x,y) = a(x,y) + c(x,y)\exp(i2\pi f_o x) + c^*(x,y)\exp(-i2\pi f_o x), \tag{2.8}$$

where

$$c(x,y) = \frac{1}{2}b(x,y)\exp\left[i\phi(x,y)\right], \tag{2.9}$$

and $*$ denotes complex conjugation. Taking the Fourier transform of Equation 2.8 with respect to the x coordinate, we obtain

$$G(f,y) = A(f,y) + C(f - f_o, y) + C^*(f + f_o, y), \tag{2.10}$$

where capital letters denote the Fourier spectra and f is the spatial frequency in the x direction. Hence, by implementation of a filter to pull out the $C(f - f_o, y)$ component to obtain $C(f,y)$, and inverse Fourier transforming it back to the spatial domain, the phase can be calculated by [36]

$$\phi(x,y) = \tan^{-1}\left(\frac{\mathrm{Im}\left[c(x,y)\right]}{\mathrm{Re}\left[c(x,y)\right]}\right) \tag{2.11}$$

where Re[·] and Im[·] represent the real and imaginary parts of ·, respectively.

2.3 Phase Unwrapping

One of the limitations of the phase analysis technique is that the phase is determined modulo 2π due to the nature of the inverse tangent function. Hence the calculated phase must be unwrapped to its true value. In many ways, this is analogous to the fringe ordering problem of intensity based methods [22, Section 4].

The inverse tangent function will provide phase values in the range $-\pi \leq \phi \leq \pi$. In the absence of noise and assuming the object is smooth and well sampled, the true phase difference between adjacent pixels will be less than π. Hence, the phase unwrapping problem becomes trivial as one only needs to look for a phase difference greater than π and add or subtract integer multiples of 2π to align the phases. Unfortunately, we do not live in a smooth, noise free world. Noise spikes occur and fades in the fringe modulation (visibility) amplify those noise effects. Further, physical discontinuities in the object, such as steps, holes, or cracks, will create regions where the true phase difference is greater than π or perhaps several multiples of π.

Phase unwrapping is the major problem facing interferometric profilometry. Several algorithms for performing phase unwrapping have been developed over the past couple decades, some of which will be summarized here. For a more thorough review, the reader is referred to references [22, 32] and [48].

The simplest unwrapping method, commonly referred to as Schafer's algorithm [43, Section 12.7.1], [63] compares the phase values of adjacent pixels in search of 2π discontinuities. The columns are unwrapped first using

$$\begin{aligned} \text{if} \quad & [I_w(i, j+1) - I_w(i, j) \approx \pm 2\pi] \,, \\ \text{then} \quad & [I_{u1}(i, j+1) = I_w(i, j+1) \mp 2\pi] \,. \end{aligned} \tag{2.12}$$

The row unwrapping is similarly performed as

$$\begin{aligned} \text{if} \quad & [I_w(i+1, j) - I_w(i, j) \approx \pm 2\pi] \,, \\ \text{then} \quad & [I_{u1}(i+1, j) = I_w(i+1, j) \mp 2\pi] \,. \end{aligned} \tag{2.13}$$

While this method works well for well–sampled and error–free fringe patterns, it is highly sensitive to noise. Since the pattern is unwrapped serially, an error at one pixel will propagate throughout the reminder of the array.

To combat this, Gierloff [17] proposed an unwrapping by regions approach in which the wrapped phase map is first segmented into regions containing no phase ambiguities. The edges of these regions are then compared and the entire region is phase shifted to remove 2π phase wraps. While this approach confined the error propagation to a single region, it had problems dealing with discontinuities, such as physical edges or holes, in the data. Charette and Hunter [7] proposed a more robust method of performing the segmentation

for phase images with high amounts of noise based on fitting a plane to the data and establishing as a "region" the connected data points that best fit that plane. Later, Hung and Yamada [21] suggested a least–squares approach to improve the phase unwrapping around physical discontinuities.

Itoh [30] showed that the true phase could be recovered by differentiating the wrapped phase map, wrapping it and then integrating. Ghiglia *et al.* [16] expanded on that idea and described a method based on cellular automata. Quoting from Ghiglia, "Cellular automata are simple, discrete mathematical systems that can exhibit complex behavior resulting from collective effects of a large number of cells, each of which evolves in discrete time steps according to rather simple local neighborhood rules." In other words, for each iteration, the phase value of each pixel is changed based upon the phase values of it neighbors. The process continues until the entire phase image converges to a steady state, which hopefully is the correct phase map. This algorithm had one serious shortcoming–it was very computationally expensive. Several thousand iterations through the array are required to unwrap even simple phase maps.

Huntley proposed a "branch cut" phase unwrapping method [3, 22] in which discontinuity sources are identified and branch cuts are placed between sources of opposite sign. Simple phase unwrapping techniques are then used, but prohibited from crossing a branch cut. This prevents potential error sources from corrupting the reminder of the phase map. Similar methods, referred to as pixel queuing, unwrap pixels with high signal–to–noise (modulation or visibility levels) levels first. These methods often use "minimum spanning tree"

or "tile processing" methods [19, 33, 63]. Unfortunately, they too can be computationally expensive.

Many other methods for phase unwrapping exist, some of which are based on discrete cosine transforms [34], Markov models [42] and regularized phase tracking techniques [56, 57, 58, 59]. However, all these methods, and the ones mentioned above, assume the maximum true phase difference between two adjacent pixels is $\leq \pi$. This condition is not met for many practical applications, especially those involving robot vision of engineering objects.

2.3.1 Unwrapping methods that accommodate step discontinuities

Huntley and Saldner proposed a temporal phase–unwrapping algorithm [23]. In this process, the phase is determined using a 4–step phase shifting [12] algorithm. Then the fringe spacing is changed and the 4-step process repeated. Each pixel is then unwrapped "temporally" using the phase maps from different fringe spacings. Later papers by these researchers expanded on the idea, including the use of a spatial light modulator to easily adjust the fringe phase and spacing [24, 25, 50, 51, 52]. Since this method unwraps each pixel individually, it has no problem handling step discontinuities in the object being profiled. Hence, unlike all the other methods which compare adjacent pixels, this method can accommodate true phase steps of greater than 2π. The main drawback of this method is the large number of frames which must be captured to perform the phase unwrapping.

Other researchers have used a similar idea, only using just two fringe patterns with different periods so as to reduce the number of required images [37, 73]. Creath [10] also used a two–wavelength system, but used the beating of the two phase patterns to obtain an even longer third wavelength. These three methods used phase–shifting techniques to obtain the phase pattern. Others used the Fourier transform technique, in which case the two spatial frequencies can be obtained by a pair of crossed gratings [6, 65, 71] and the phase information separated in frequency space. Hence only one fringe image is required. In all these methods, the lower frequency fringe pattern is used to unwrap the higher frequency pattern–which also has higher depth resolution.

Chapter 3 System Design and Manufacturing

As described in Chapter 2, several surface mapping systems, or profilometers, are already in existence and performing very well. However, most of them can also be rather large and bulky due to the complicated optical setup. For operation on a mobile robot or in small spaces, a different approach is necessary that allows smaller optics and a remote location of the light source. One of the primary reasons for the bulkiness of the other systems is their use of collimated light or fringe patterns. This required the fringe projection system to be larger than the surface being mapped.

The system developed during this research is depicted in Figure 3.1. The heart of the system is the fringe generator which consists solely of a two by two single mode 633nm 3dB fiber coupler. The coupler is pigtailed to the laser source through a fiber cable. Also in the "sensor head module" along with the fringe generator is a CCD camera. Fringes are projected from the generator to the object and then viewed with the CCD camera. The locations of the fringes are governed by the equation:

$$I(x,y) = 2I_o(x,y)\left[1+\cos\left(\frac{2a}{D}kx-\Delta\phi\right)\right] \tag{3.1}$$

where $2a$ is the separation between the fibers (or pinholes), D is the distance from the pinholes to the object, $k = 2\pi/\lambda$, λ is the wavelength, and $\Delta\phi$ accounts for any phase difference at the endfaces of the two fibers. Hence, we can see that the fringe pattern is dependent on the

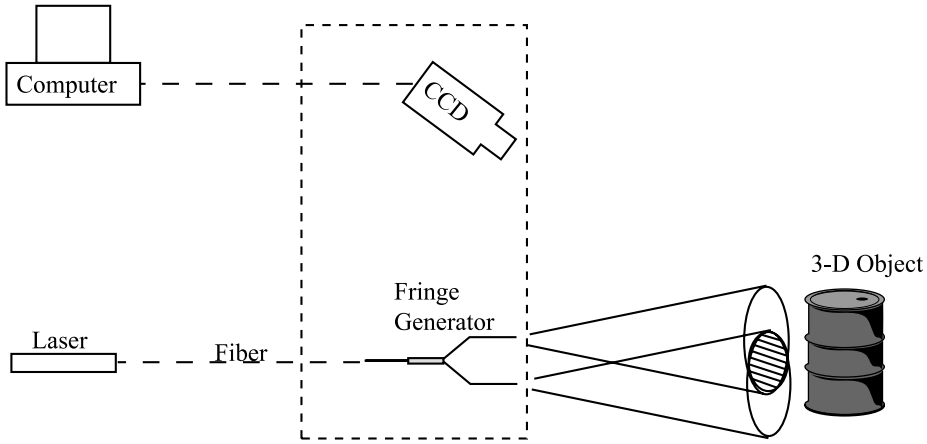

Figure 3.1. Top–level system description

distance to the object, which is a function of the object's surface profile. It should be noted that Equation 3.1 is based on the paraboloidal approximation to the spherical wave [53], which assumes that $\sqrt{x^2 + y^2} \ll d_p$. Examples of the fringe pattern on a flat surface and a triangular shaped object are provided in Figure 3.2. This fringe pattern is viewed by the CCD camera and sent to a Pentium class computer for processing. The 3–D shape of the object is then determined from the phase of the fringes as described in Section 3.1. Due to the nature of determining the phase values, they are "wrapped" modulo 2π and must be "unwrapped" to their true phase values. The method used to perform this unwrapping is described in Section 3.2. An analysis of various system parameters and estimates of the system resolution is provided in Section 3.3, while the manufacturing process is described in Section 3.4.

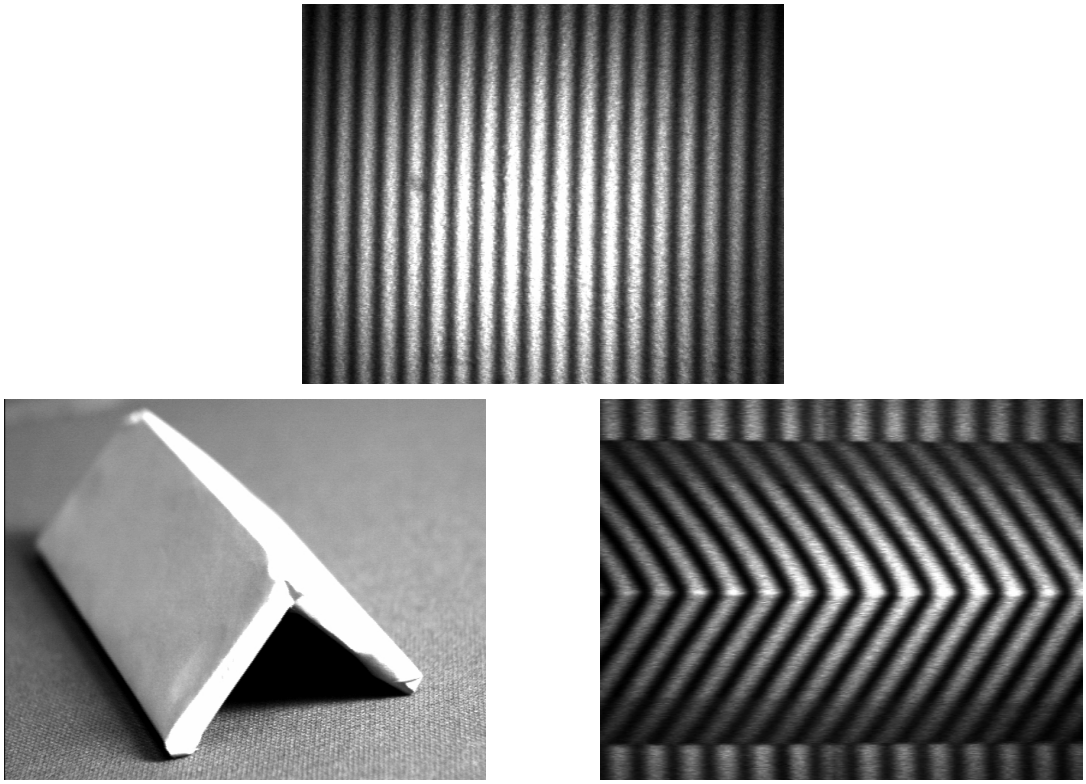

Figure 3.2. Example of fringe pattern on a flat object and on a triangular object

3.1 Mathematical Model of Fringe Projector

The main goal in modeling the fringe projector and resulting fringes is to obtain the relationship between the fringe position, or phase, and the height profile of the surface. That is, we seek to find the function, f, such that

$$h(x, y) = f\left[\phi(x, y)\right], \tag{3.2}$$

where $\phi(x, y)$ is the phase of the fringe pattern as observed from the camera and $h(x, y)$ is the height profile of the object.

Let us begin by establishing the coordinate system as defined by Figure 3.3. The pinhole and object coordinate systems are shown here where the camera is aligned along the object's z_o axis. The viewing angle β is defined as

$$\tan\beta = \frac{L}{d} \tag{3.3}$$

where $\sqrt{L^2 + d^2}$ defines the distance between the fiber pinholes and the origins of the pinhole and object coordinate systems. Since our measurable quantity is defined by the camera pixels, we will express each coordinate as a function of camera pixel number, (m, n). The phase for each pixel, assuming $\Delta\phi = 0$, is then given by

$$\phi(m, n) = k\frac{2a}{D(m, n)}x_p(m, n); \tag{3.4}$$

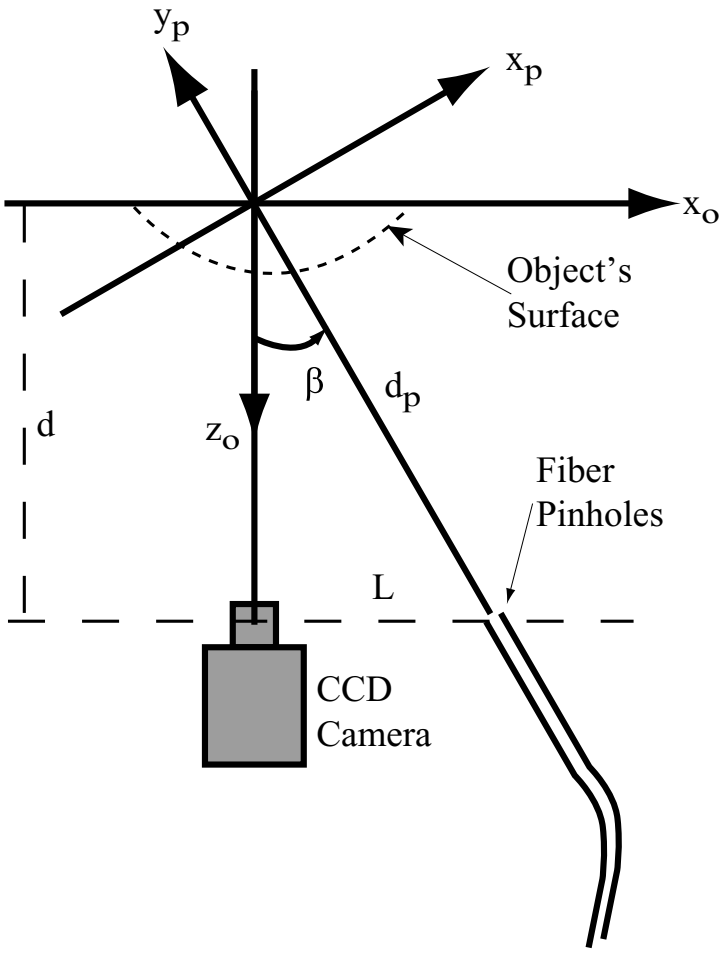

Figure 3.3. Coordinate Systems

where $k = 2\pi/\lambda$ is the wave number, λ is the wavelength, $2a$ is the separation of the fiber (pinhole) centers and $D = d_p + y_p$ is the distance from the pinholes to the object's surface. The fringe period (spacing) is given by

$$P_o = \frac{\lambda D(m,n)}{2a}. \tag{3.5}$$

Referring to Figure 3.3, x_p can be expressed in terms of the object's coordinate system as

$$x_p = z_o \sin\beta + x_o \cos\beta, \tag{3.6}$$

thus the phase can be related to the object's surface as

$$\phi(m,n) = k\frac{2a}{D(m,n)}\left[z_o(m,n)\sin\beta + x_o(m,n)\cos\beta\right]. \tag{3.7}$$

If we were using collimated fringes, we would have the desired relationship for Equation 3.2 at this point. That is, we could easily manipulate Equation 3.7 to express $z_o(m,n)$ in terms of $\phi(m,n)$. However, since we do not have collimated fringes, P_o becomes a function of both x_o and z_o. The distance to the object can be expressed as

$$D(m,n) = d_p + y_p(m,n) \rightarrow P_o(m,n) = \frac{\lambda}{2a}\left(d_p + y_p(m,n)\right), \tag{3.8}$$

where y_p can be considered the height of the object in the pinhole coordinate system. Again referring to Figure 3.3, y_p can be translated to the object's coordinates using $y_p = x_o \sin\beta -$

$z_o \cos\beta$. Equation 3.7 now becomes,

$$\phi(m,n) = \frac{k2a\left[z_o(m,n)\sin\beta + x_o(m,n)\cos\beta\right]}{d_p + x_o(m,n)\sin\beta - z_o(m,n)\cos\beta}. \tag{3.9}$$

Using the relationship that $d_p = d/\cos\beta$, we get

$$\phi(m,n) = \frac{k2a\left[z_o(m,n)\sin^2\beta + x_o(m,n)\cos\beta\sin\beta\right]}{L + x_o(m,n)\sin^2\beta - z_o(m,n)\cos\beta\sin\beta}. \tag{3.10}$$

Solving for z_o can now be easily done:

$$z_o(m,n) = \frac{\phi(m,n)\left[L + x_o(m,n)\sin^2\beta\right] - k2ax_o(m,n)\cos\beta\sin\beta}{\phi(m,n)\cos\beta\sin\beta + k2a\sin^2\beta}. \tag{3.11}$$

With this expression, we have established the relationship between the phase of the fringe pattern and the surface profile. Hence, our surface mapping system becomes a matter of fringe projection, imaging, and phase determination.

3.2 Phase Determination and Unwrapping

In Chapter 2, two methods were described for determining the phase of a fringe pattern. The first was phase–shifting interferometry and the second was Fourier transform fringe analysis. While phase–shifting interferometry is usually the preferred method, it requires capturing several fringe patterns (usually three or four), each with a different phase shift. This phase shift must be precisely controlled for the method to work well. The Fourier transform method only requires one fringe pattern and hence does not require the precise phase shifting. It was selected as the phase determination method.

An example of this process is shown in Figure 3.4. A representative portion of a fringe pattern on a flat object is shown in Figure 3.4(a). This pattern is Fourier transformed and its modulus is shown in Figure 3.4(b), along with a Gaussian filter centered on the frequency which corresponds to the carrier frequency, or average fringe period. This filter eliminates all other frequency components. This filtered spectrum is then inverse Fourier transformed and Equation 2.11 is used to determine the phase for every point, as shown in Figure 3.4(c). As discussed in Section 2.3, Equation 2.11 returns the value of the phase modulo 2π. For simple objects like this, the phase can be unwrapped using a method similar to that described by Schafer [43]. The unwrapped phase is shown in Figure 3.4(d).

For more complicated objects, phase unwrapping is perhaps the most challenging task of the profiling process. A review of current methods of performing phase unwrapping was provided in Section 2.3. The approach chosen for this research was different. Two

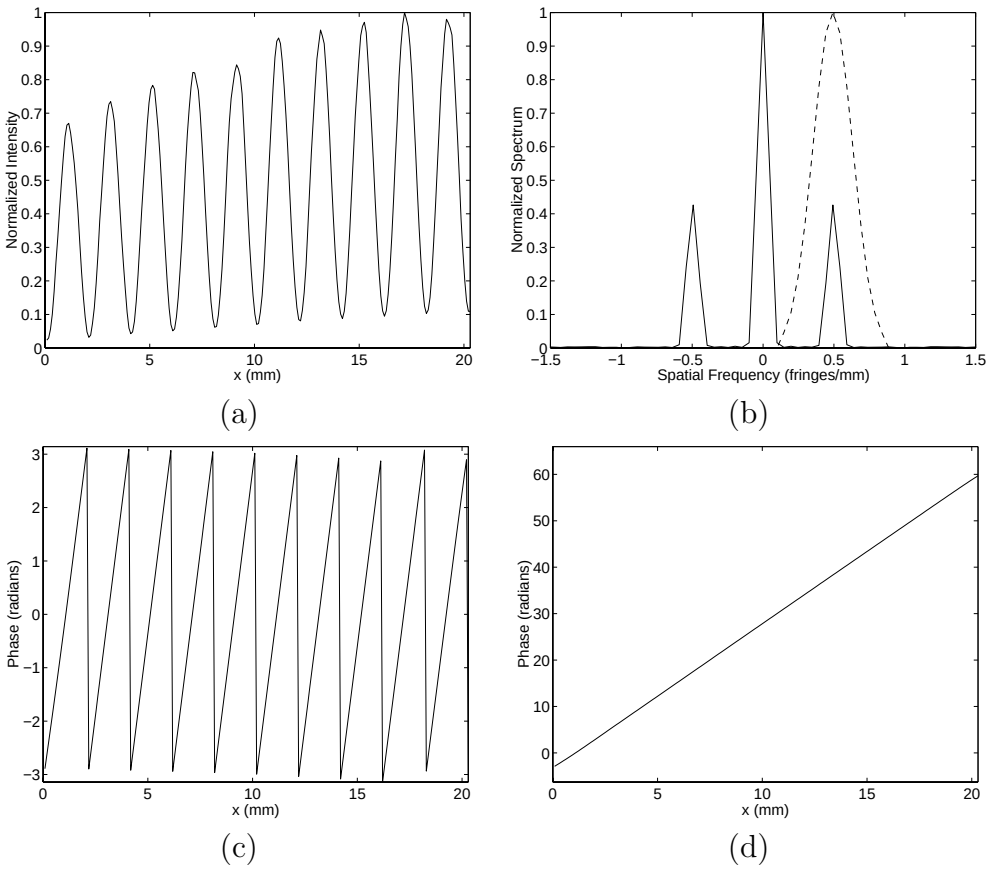

Figure 3.4. (a) Representative fringe pattern. (b) Modulus of the spectrum of the fringe pattern (solid line) and the filter (dotted line) used to pull out one of the peaks. (c) Modulo 2π wrapped phase determined using Equation 2.11. (d) Unwrapped phase.

wavelengths (633nm–HeNe and 833nm–laser diode) were sequentially projected through the fiber pinholes, providing two fringe patterns with slightly different fringe periods. The lengths of the fibers were carefully controlled, as will be described in Section 3.4, so that the zero order fringe will be in the same position for both fringe patterns, *i.e.*, $\Delta\phi = 0$ in Equation 3.1. The phase is then unwrapped using the *unwrap* function in *Matlab* version 5.3. The algorithm used by this function is similiar to the method proposed by Itoh [30]. The phase of each row is corrected by shifting the phase of each row so that the phase is zero at the zero order fringe location. This corrects for any step discontinuities along the zero order fringe.

3.3 System Analysis

In this section, we will explore various parameters that are key to maximizing the performance of the three-dimensional profilometer. First we will explore the optimum viewing angle, β as shown in Figure 3.3. Next we will explore the fringe generator subsystem. Lastly we will determine the laser power requirements based on the sensitivity of the camera.

3.3.1 Optimum Viewing Angle

The optimum viewing angle is the one that maximizes the phase sensitivity so that small changes in the object's height will generate measurable fringe pattern shifts. We can determine the optimum viewing angle by using Equation 3.11 to find $\mathrm{d}z_o/\mathrm{d}\phi$ and computing the value of β that minimizes this derivative. A more intuitive result, however, can be found by

assuming collimated fringes and using Equation 3.7 instead. Doing so, we obtain

$$\frac{\mathrm{d}z_o}{\mathrm{d}\phi} = \frac{P_o}{2\pi \sin\beta}, \tag{3.12}$$

where P_o is the fringe spacing given by Equation 3.5. This equation is plotted in Figure 3.5. For this plot we assumed the minimum detectable phase difference was $2\pi/100$ based on the expected number of gray levels between the peak and valley of the fringes imaged onto a CCD camera with an eight bit digitizer.[1] While this plot shows that the system resolution will continue to improve with a larger viewing angle, there are advantages to keeping the viewing angle small. The two primary advantages are the reduction of signal fades due to shadows on the object and an increase in light reflected towards the camera. Hence a viewing angle of 10 to 15 degrees is planned. The results presented in Chapter 4 used a viewing angle of 14 degrees and a distance of one–half meter. From Figure 3.5, we would expect a resolution of about 0.1mm. A rigorous analysis, starting from Equation 3.11, is provided in Appendix A.

3.3.2 Fringe Generator Subsystem

To achieve the best performance, we desire high visibility fringes. Maximum fringe visibility will be achieved if the power and polarization of the light exiting each fiber is identical.

[1]Ideally, we should expect the number of gray levels to be 256 for an eight–bit digitizer. However, experience with the camera/frame grabber being used for this research indicates that a more practical assumption is 100 gray levels.

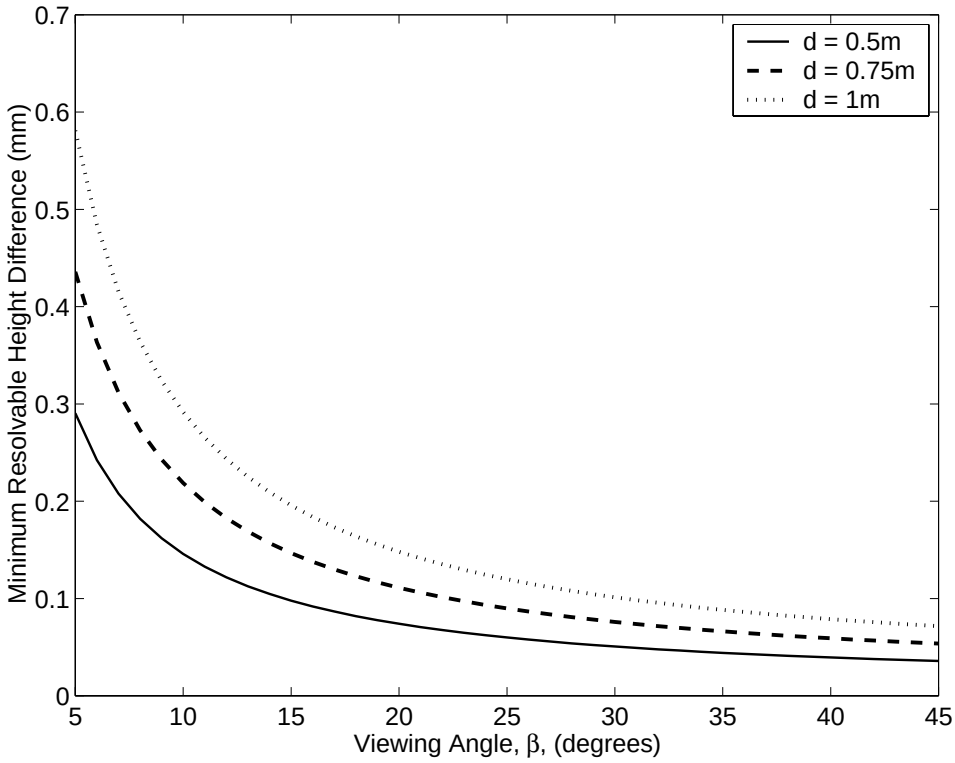

Figure 3.5. Minimum detectable height variation (resolution) as a function of viewing angle for several different object distances, d.

However, recall from Section 3.2 that we plan to use two wavelengths to aid in the phase unwrapping and to find the zero order fringe. Hence, we need to use a coupler designed to provide a 50/50 splitting ratio at both wavelengths. We can ensure the polarization is the same by minimizing the bending and twisting of the fiber after the coupling region of the 2x2 fiber coupler.

Furthermore, two wavelength operation requires that the phase difference of the light exiting each pinhole to be nearly zero (modulo 2π) at both wavelengths. This is equivalent to setting $\Delta\phi = 0$ in Equation 3.1. However, if the fibers from the coupler to the "pinholes" differ in length, or if the fiber endfaces are not perfectly aligned, then $\Delta\phi$ will be wavelength dependent, given by

$$\Delta\phi(\lambda_1, \lambda_2) = 2\pi \left[n_f \Delta L - n_o d\right] \left(\frac{\lambda_1 - \lambda_2}{\lambda_1 \lambda_2}\right) + \frac{2\pi}{\lambda_2} \Delta n \Delta L. \tag{3.13}$$

Here, $\Delta\phi$ is the phase difference between the two fibers at λ_1 minus the phase difference between the two fibers at λ_2, where λ_1 and λ_2 are the two wavelengths used to calculate the zero order fringe, $n_f = n(\lambda_1)$ is the effective refractive index of the fiber core at λ_1, $\Delta n(\lambda_1, \lambda_2) = n(\lambda_2) - n(\lambda_1)$ is the change in refractive index due to dispersion, n_o is the refractive index of air, and d is the offset between the two fibers endfaces illustrated in Figure 3.6. L_1 is the length of the longer fiber, L_2 is the length of the shorter fiber and ΔL is defined as $\Delta L = L_1 - L_2$.

To ensure the phase difference is zero (or at least an integer multiple of 2π), we must

carefully control both ΔL and the offset, d, between the fiber endfaces. How precisely this length difference and offset must be controlled is important to determine.

A criterion was established that the zero order fringe (imaged onto the CCD camera) must move less than one pixel when the source wavelength is switched. From examining the optical setup, there will be less than 30 pixels per fringe period. Hence, the phase difference, $\Delta\phi$, must be less than $2\pi/30$. This will ensure that the zero order fringe moves less than one pixel when the source wavelength is switched.

Looking again at Equation (3.13), if dispersion is neglected ($\Delta n = 0$), any small length difference could be easily compensated for by adjusting the offset between the fiber endfaces so that $d = n_f \Delta L / n_o$, as illustrated in Figure 3.6. We note that d must still be less than 0.5mm so that the light diverging from the short fiber endface does not intersect the long fiber. If we include the effects of dispersion and adjust the fiber offset as described, then the $[\cdot]$ term in Eq. (3.13) goes away and we can determine the maximum fiber length difference as

$$\Delta L_{\max} = \frac{\lambda_2 \Delta\phi_{\max}}{2\pi\Delta n}. \tag{3.14}$$

Using Reference [14, pg. 7–85, Table 16], Δn was determined to be 4.2×10^{-3}. Setting $\Delta\phi_{\max} = 2\pi/30$, the maximum fiber length difference we can tolerate is 6.6μm.

Another factor that must be considered is the effects of temperature fluctuations which will make controlling the fiber length difference more difficult. Ambient temperature fluctuations could possibly cause temperature differences between the two fibers and hence optical

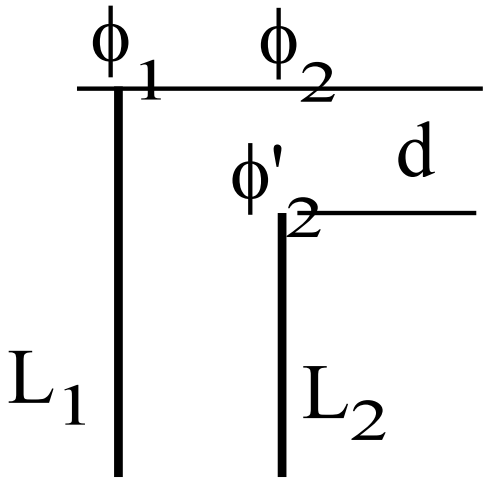

Figure 3.6. Schematic of the fiber alignment used to compute the optical path difference using Equation (3.13). L_1 is the length of the long fiber, L_2 is the length of the short fiber, d is the normal distance between two lines parallel to the fiber endfaces, ϕ_1 is the phase of the light exiting the long fiber, ϕ_2' is the phase exiting the short fiber and ϕ_2 is the phase of the short fiber's light when it is parallel to the long fiber endface.

length differences. The phase difference arising from temperature gradients can be estimated using

$$\Delta\phi \approx \frac{2\pi}{\lambda} n_f L (C_L + C_n) \Delta T, \tag{3.15}$$

where n_f is the effective refractive index of the fiber core, L is the length of the fiber after the coupling region, ΔT is the average temperature difference between the two fibers, $C_L = 5 \times 10^{-7}$in/in°C is the coefficient of thermal expansion for silica glass [35], and $C_n = 3 \times 10^{-5}$/°C is the dependence of the index of refraction on temperature [14, pg. 8–72]. Equation 3.15 is plotted in Figure 3.7 versus ΔT for several different post–coupler fiber lengths. Even modest temperature differences can create a large phase difference, especially as the post–coupler fiber length grows. To control this, we must strive to minimize the length of the fiber between the coupler and the pinholes, which will also serve to reduce the effects

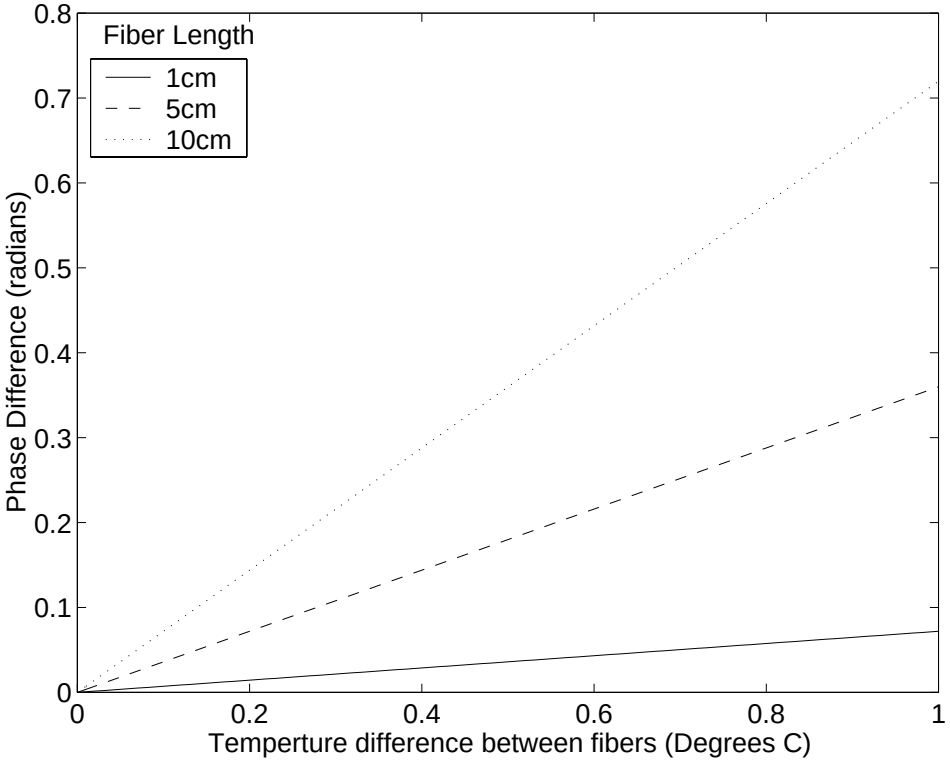

Figure 3.7. Sensitivity of the phase difference to temperature differences between the fibers. We desire to keep the post–coupler fiber lengths short to minimize this effect.

of mechanical vibration and polarization rotation. Another method to reduce this effect is to encase the post–coupler fibers inside an insulated structure, such as a ceramic tube. This could also help reduce the effects of mechanical vibration.

If we assume that such an insulating tube is encasing the fibers so that they remain at the same temperature, then any ambient temperature shifts will only affect the phase if the fibers are of unequal length. It was shown earlier in this section that the length difference must be less than 6.6μm to satisfy the requirements of using dual wavelengths. Assuming that requirement is barely met, then the sensitivity to temperature can again be estimated

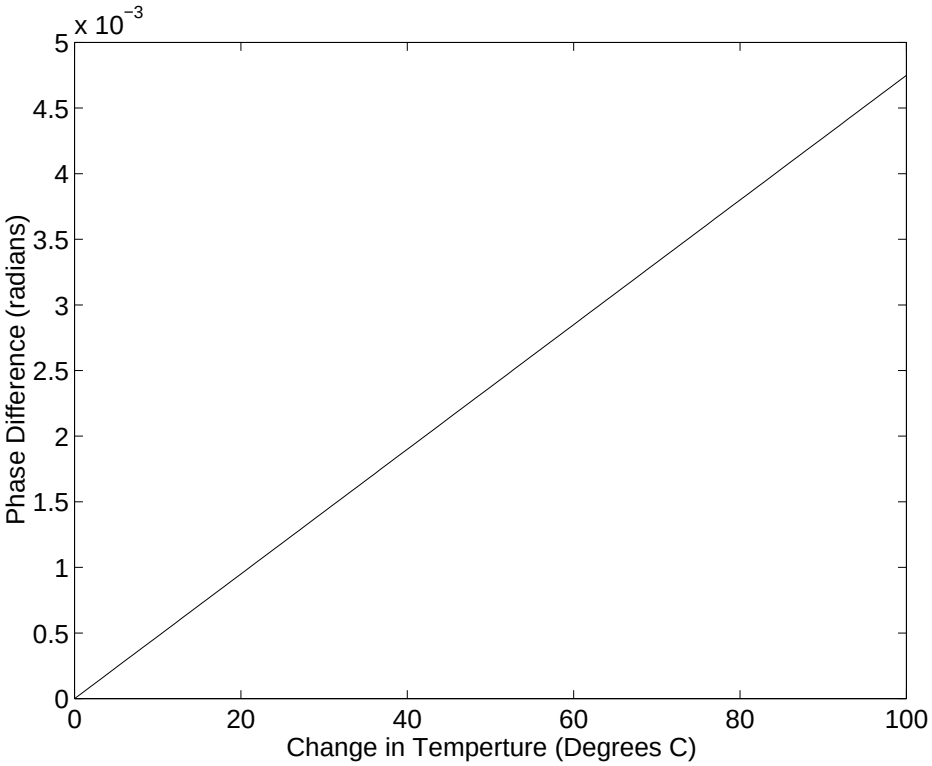

Figure 3.8. Sensitivity of the phase to ambient temperature variations. In this figure, we assume the two fibers are at the same temperature, but differ in length by 6.6μm, as specified earlier in this section to met the dual wavelength requirements.

using Equation 3.15 by replacing L with $\Delta L = 6.6\mu$m. This effect is plotted in Figure 3.8. For this case, even large temperature variations have very little effect on the phase of the fringe pattern.

3.3.3 Camera and Laser Subsystems

In the camera and laser subsystems, the parameter we are most concerned about with the camera is its sensitivity, or how much light must be reflected from the object for the camera

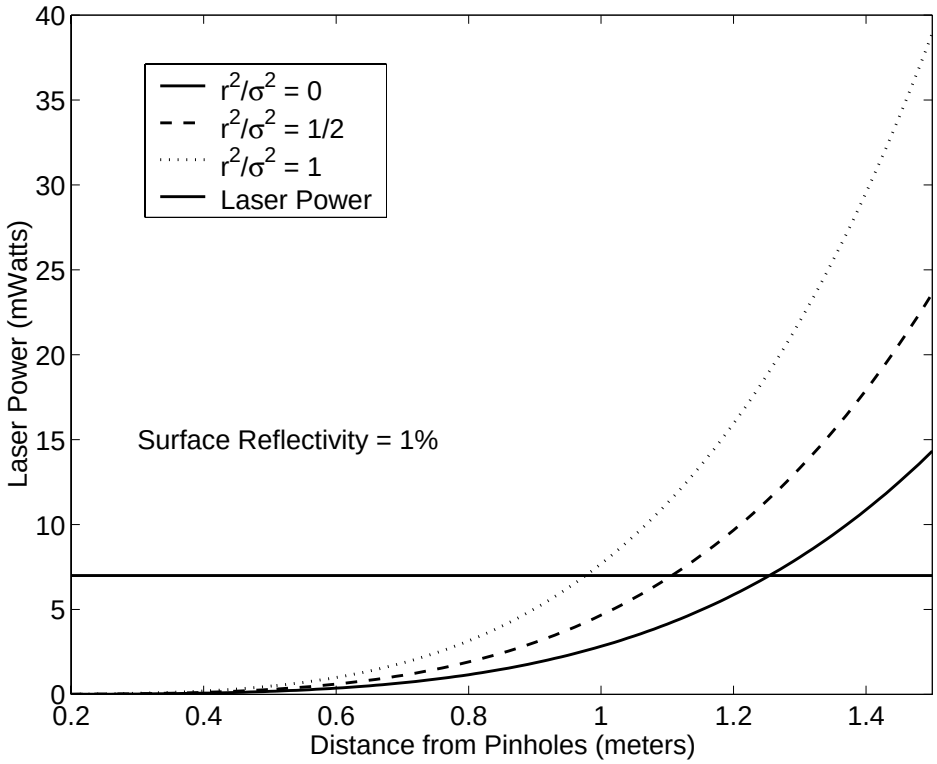

Figure 3.9. Required laser power for the camera to detect the reflected fringe pattern from a surface with a surface reflectivity of 1%. The curves represent different points along the distribution from the center $r^2/\sigma^2 = 0$ to the edge of the distribution $r^2/\sigma^2 = 1$. σ is defined as the width of the distribution as determined by the critical angle of the fiber, $\sigma = d\tan(\theta_c)$. Also shown is the power of the laser being used.

to properly detect the fringes. This directly translates to the required laser power. A plot of this required laser power versus distance of the object from the fibers is given in Figure 3.9. For this plot, a camera sensitivity of 0.5 Lux was used (as specified for the Sony XC-75 CCD camera without the IR cutoff filter). Further, we used a surface reflectivity of 1%, which was measured from a white matte surface at approximately 15°. From Figure 3.9, we can see that, given the available laser power, the maximum operating range for full mapping is approximately 1 meter. Between 1 and 1.2 meters, the mapping area is reduced. The system

will not work beyond 1.2 meters unless the laser power or the surface reflectivity is increased.

This will also effect the system resolution as discussed in Section 3.3.1. As the reflected power decreases, so will the difference between the intensity levels of the peaks and valleys of the fringe pattern. This will reduce how accurately the phase can be determined and will, in turn, decrease the resolution.

3.4 Manufacturing Process

The goal of the manufacturing process is to construct a Young's double pinhole interferometer that meets the requirements set forth in Section 3.3. The most stringent requirement, in order to use the zero order fringe as a calibration line, was to ensure that the position of the zero order fringe was not wavelength dependent. This proved to be a very challenging portion of this research.

Several methods were attempted to construct a double pinhole interferometer to meet the requirements of Section 3.3. First, a commercial–off–the–shelf (COTS) coupler was ground down and polished until the fibers were adjacent. This did not work because, while the fibers were adjacent, the light coming out of the two fibers was diverging, as will be described below in Section 3.4.1. Next, the leads out of a COTS coupler were polished individually in an attempt to equalize the lengths. A white–light–interferometer [38] was used to measure the length difference. This method did not work because the splitting ratio of the COTS coupler was not close enough to 50/50 to allow fringes to be visible

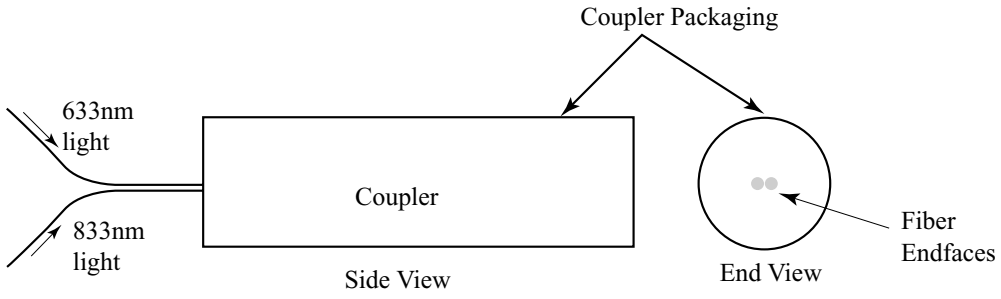

Figure 3.10. Illustration of the first attempt to manufacture a fiber optic Young's interferometer.

on the white–light–interferometer. Hence a thermally fused biconical tapered coupler was manufactured using a method described in reference [69]. The process of making couplers, along with measurements of the splitting ratio and estimated loss, is described below in section 3.4.2. This coupler was then polished using a white–light interferometer until the difference in the fiber lengths was approximately 6μm. This process is summarized in [44], and described in Section 3.4.3 in more detail. Finally, the fibers were aligned and bonded together as described in Section 3.4.4.

3.4.1 Initial Attempt to Polish a Standard Coupler

The first attempt to make a fiber optics Young's double pinhole interferometer was an intuitively simple concept. A COTS coupler was cut and the fiber and packaging was polished away until the fibers were adjacent as shown in Figure 3.10. The coupler was polished using an Ultra Tec polishing machine available at the Photonics Laboratory. Incrementally during

the polishing, the coupler endface would be examined under a microscope to determine if the fibers were touching. Also, the fringe pattern would be projected onto a flat surface and examined. During this process, two disturbing trends were observed. First, even though the fibers were moving closer together, the intensity patterns observed on a flat surface were not, as seen in the top two photos of Figure 3.11. That is, the intensity pattern from one fiber was not overlapping with the intensity pattern from the other fiber–a necessary condition for creating high visibility fringes. Second, the orientation of the fringes was not perpendicular to the bi–sector joining the two intensity patterns, as we would expect from Equation 3.1. This can be observed in the top right photo of Figure 3.11. We also note in Figure 3.11 that the orientation of the fibers appears to be rotating slightly. This observation lead to determining the cause of the fringe pattern rotation as well.

During the coupler manufacturing process, the fibers are twisted together and then heated as they are stretched. Thus, if the coupler has been ground away to a point where the fibers are twisted around each other, then the polishing will introduce an angle on the endface of one fiber relative to the other. This, I suspected, could cause the diverging intensity patterns, and perhaps the rotation in the fringe patterns as well.

A model was developed for the intensity pattern out of each fiber using the mode field distribution inside the fiber as a guide. The transverse mode field distribution is given by [1]:

$$e_x = \begin{cases} \frac{-j}{u}\beta A J_0(ur), & r < a \\ \frac{-j}{w}\beta A \xi K_0(wr), & r > a \end{cases} \tag{3.16}$$

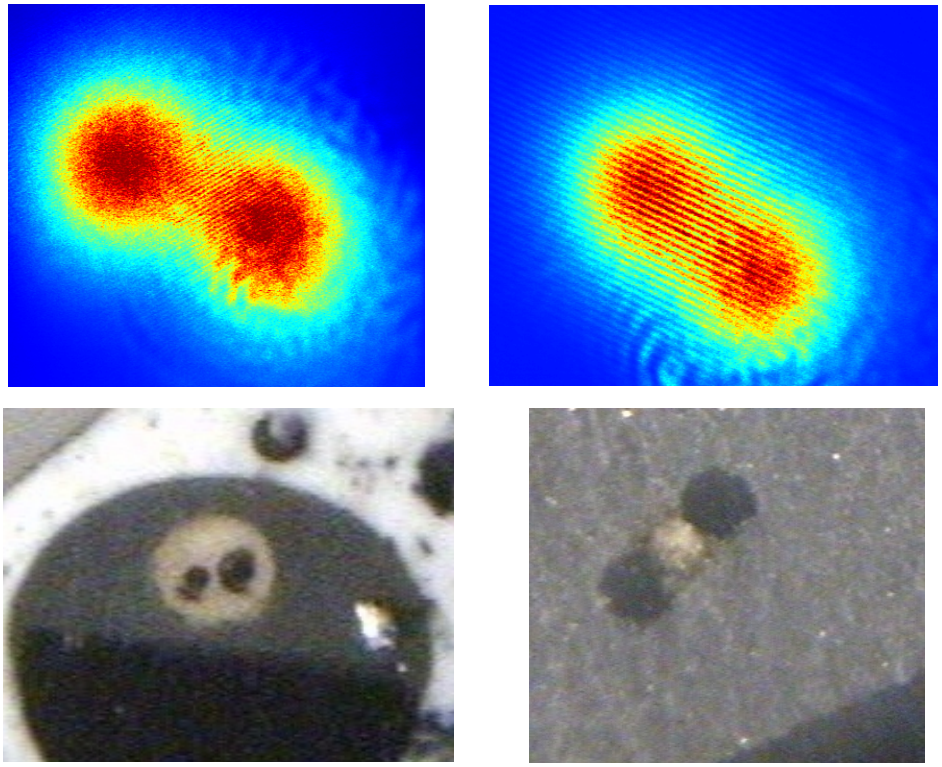

Figure 3.11. Fringe Pattern and Coupler Endface images. The images in the right column were taken after approximately 0.4mm had been polished away from the coupler since the images in the left column were taken

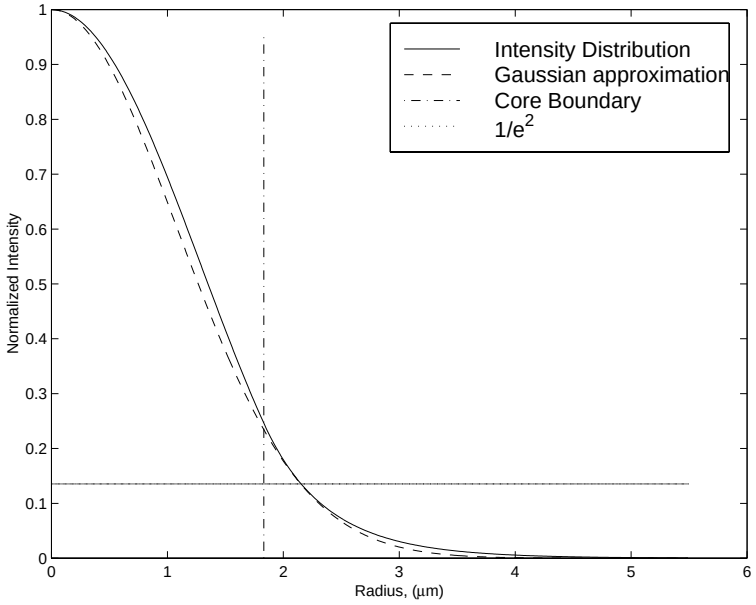

Figure 3.12. Comparison of the intensity distribution inside a single mode 633–nm fiber and a Gaussian approximation

where J_0 is a Bessel function of the first kind and order 0, K_0 is a modified Bessel function of the second kind and order 0, r is the radial component, a is the core radius, ξ is a scaling factor resulting from the boundary conditions, and $j = \sqrt{-1}$. The normalized frequency variables are defined as $u^2 = a^2\left(k^2 n_1^2 - \beta^2\right)$, and $w^2 = a^2\left(\beta^2 - k^2 n_1^2\right)$, where n_1 is the index of refraction of the core, n_2 is the index of refraction of the cladding, and β is the longitudinal propagation constant. For computational ease, the intensity distribution can be well modeled as a Gaussian distribution by matching the $1/e^2$ points of Equation 3.16 and the Gaussian. A comparison of the two distributions is shown in Figure 3.12

This Gaussian distribution is then used to model the intensity distribution out of each fiber on the coupler endface, or aperture function, as shown in Figure 3.13. Note that the

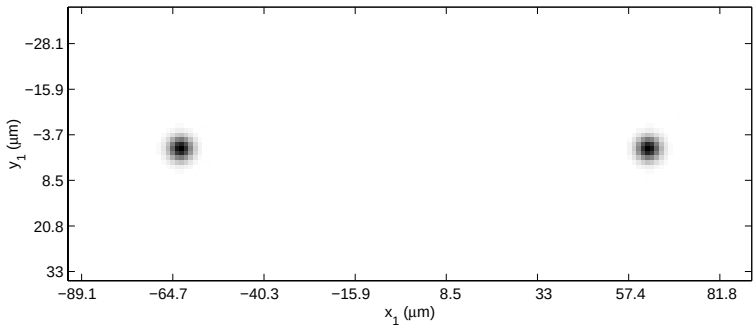

Figure 3.13. Intensity distribution from modeled coupler as a Young's Pinhole Interferometer

spacing of the distributions is $125\mu m$ apart. A wedge phase delay is placed on one of the pinholes using:

$$\Delta\phi = \frac{2\pi n}{\lambda}\left(x\tan\theta\cos\vartheta + y\tan\theta\sin\vartheta\right) \tag{3.17}$$

where θ is the wedge angle and ϑ is the orientation of the wedge ramp with respect to the x axis.

The intensity distribution on the observation screen is then calculated using Fresnel wave propagation, which can be expressed as [18]:

$$\begin{aligned} U_o(x_o,y_o) &= \frac{\exp(jkz)}{j\lambda z}\exp\left[j\frac{k}{2z}\left(x_o^2+y_o^2\right)\right]\iint_{-\infty}^{\infty}\{U_1(x_1,y_1) \\ &\times \exp\left[j\frac{k}{2z}\left(x_1^2+y_1^2\right)\right]\Bigg\}\exp\left[-j\frac{2\pi}{\lambda z}\left(x_o x_1+y_o y_1\right)\right]\mathrm{d}x_1\mathrm{d}y_1. \end{aligned} \tag{3.18}$$

where U_o is the field at the observation plane, (x_o, y_o) are the observation plane spatial coordinates, $U_1(x_1, y_1)$ is the field immediately after the aperture, (x_1, y_1) are the aperture spatial coordinates, $k = 2\pi/\lambda$ is the wave number, and z is the distance from the aperture

to the observation plane. In this expression, U_1 is defined to include the effects of the wedge phase delay. We note that the last term inside the integral is essentially a Fourier transform kernel. Hence, the intensity distribution at the observation screen can be determined as the Fourier transform of the aperture, multiplied by the appropriate phase terms.

Figure 3.14 shows the intensity distribution at the observation screen calculated in this manner. For this instance, $\theta = \vartheta = 0$, i.e. no wedge on the pinholes. This corresponds exactly to what we would expect from Equation 3.1. Figure 3.15 shows the intensity distribution for $\theta = 5^\circ$ and $\vartheta = 0$. Here we see that the intensity distributions from the two fibers begin to diverge. In Figure 3.16, θ is the same, but ϑ now equals 90 degrees. This corresponds very well to what we observed in the upper right photo of Figure 3.11.

Hence we can conclude that the fibers are twisted inside the coupler and that the polishing process is inducing a wedge on one fiber (pinhole) with respect to the other pinhole.

Polishing on the coupler was continued in hopes that the fibers would straighten out before the main coupling region was reached. However, high order spatial terms were soon observed in the intensity output of the fibers. This indicated that the fibers had been polished down to the coupling region, which is a multimode region [41]. In addition, the intensity levels of the fringe patterns dropped to unacceptable levels. It is believed that this was caused by water contamination of the fibers inside the coupler resulting from the polishing process.

Instead of attempting to polish another coupler as described above, it was decided to

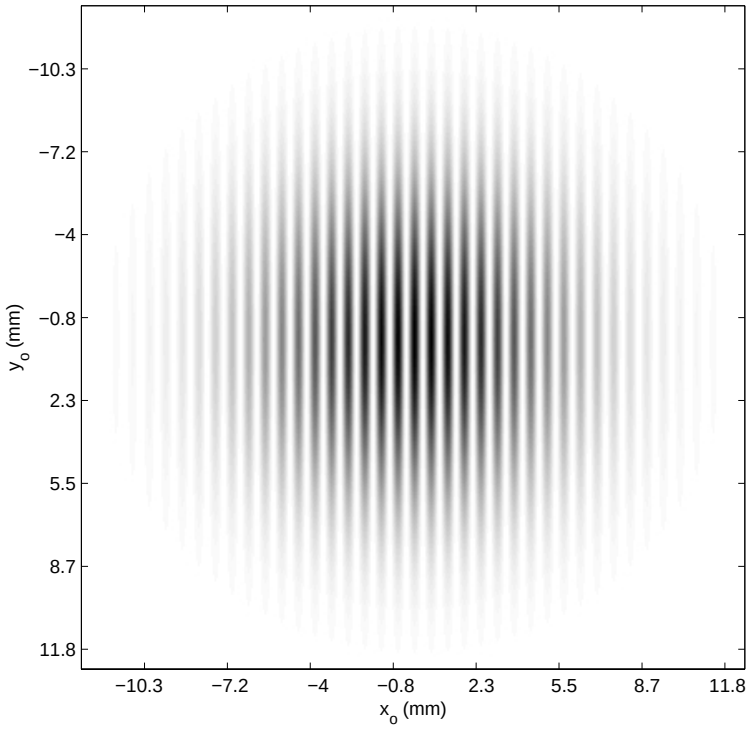

Figure 3.14. Fringe pattern calculated from Fresnel wave propagation without a wedge on one pinhole.

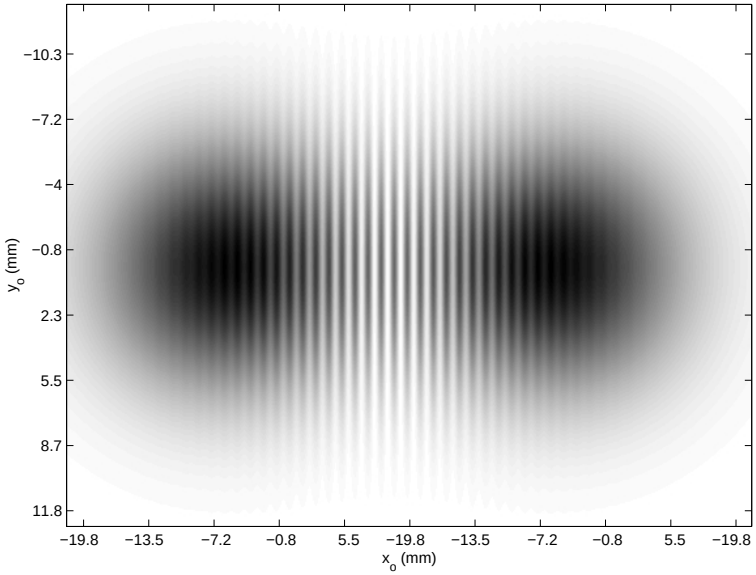

Figure 3.15. Fringe pattern calculated from Fresnel wave propagation with a wedge angle of 5 degrees on one pinhole.

attempt to polish the output leads of a coupler instead. If the length difference could be measured in a precise manner (*i.e. by a white–light–interferometer*), then the fibers could be cut so that one is longer than the other and the longer one is polished until it is the same length as the fiber cut shorter. This was attempted with a commercial–off–the–shelf coupler. However, the 633nm single mode coupler obtained this time from our source (Newport) did not have an adequate splitting ratio at 850nm, which was the wavelength used by the white–light–interferometer. Hence, it was decided that the coupler should be made in house so that an adequate splitting ratio at both wavelengths could be guaranteed.

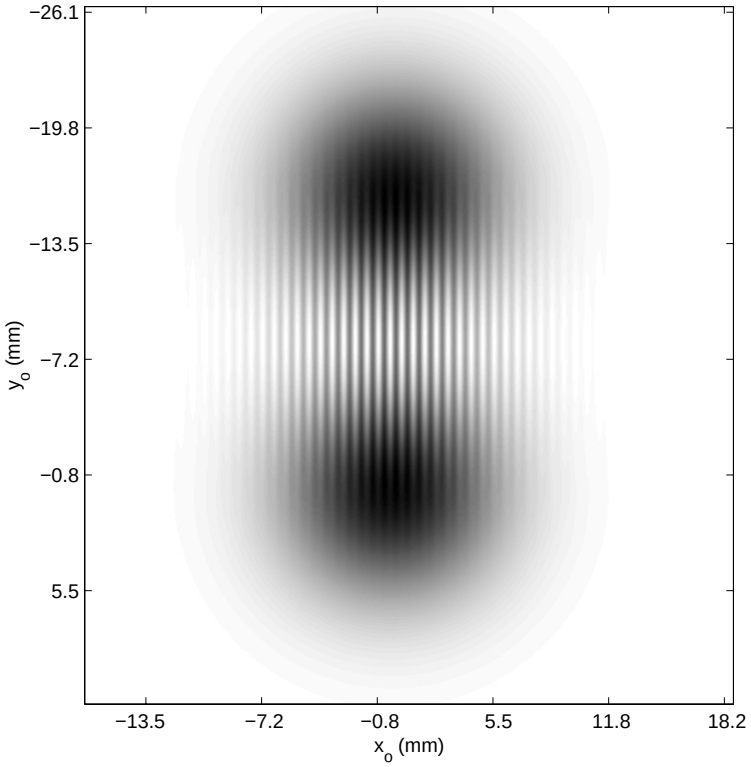

Figure 3.16. Fringe pattern calculated from Fresnel wave propagation with a wedge angle of 5 degrees, rotated by 90 degrees on one pinhole.

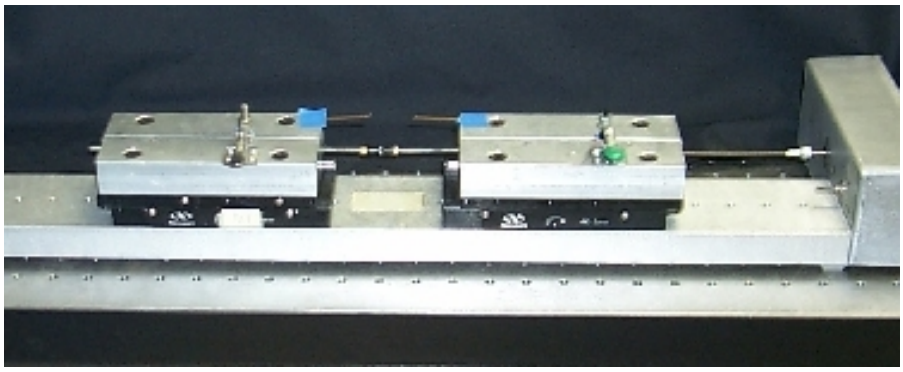

Figure 3.17. The coupler manufacturing station used to make the coupler in this system.

3.4.2 Manufacturing of a 50/50 coupler at two wavelengths

The thermally fused biconical tapered coupler was manufactured as described above in Section 3.4.1 and in References [44] and [69]. Briefly, two fibers are connected to the two sources. A small section of the fibers are stripped of their jacket and buffer, and twisted together. Using a propane torch, the fibers are then heated and pulled so that they are tapered and fused together. The power out of each fiber is monitored in real time so that the tapering process can be stopped when the splitting ratio is approximately 50/50. The coupler manufacturing station I used is shown in Figure 3.17.

After several attempts, a coupler was manufactured with 633nm single mode fiber. The loss was measured at 2dB – defined as $-10\log_{10}\left(\sum P_{\text{out}}/P_{\text{in}}\right)$ – and the splitting ratio was estimated at 1.5:1 for HeNe and 6.7:1 for the laser diode (830nm). While the loss and splitting ratio were not ideal, they were adequate to use in the system. The splitting ratios given above yield a fringe visibility of 98% for HeNe and 67% for the laser diode. For this

instance, visibility is defined as:

$$V = \frac{2\sqrt{I_1 I_2}}{I_1 + I_2}, \tag{3.19}$$

where I_2 and I_2 are the intensities of the light exiting the two fibers.

3.4.3 Polishing Specialized Couple using White–Light–Interferometer

To ensure the lengths of the two fibers are approximately equal, a white light interferometer is used, as shown in Figure 3.18. This is essentially a fiber optic Michelson interferometer with a broad spectrum superluminescent light emitting diode (SLED) source to inject light into the coupler [38]. The back reflections are then observed by an Ando optical spectrum analyzer. Fringes will develop on this spectrum corresponding to the path difference, which can be measured using:

$$\Delta L = \frac{\lambda_1 \lambda_2}{2n\,|\lambda_1 - \lambda_2|}, \tag{3.20}$$

where λ_1 and λ_2 are the wavelengths of any two adjacent peaks of the fringe pattern on the spectrum. In our setup, the two post–coupler fibers are cut so that one is approximately 1mm longer than the other. The two fibers are then mounted onto a polishing machine so that the pressure of each fiber against the lap can be controlled (see Figure 3.19). The white light interferometer is then used to measure the length difference while the longer fiber is polished.

Two spectra obtained during the polishing are shown in Figures 3.20 and 3.21. Figure 3.20 is the initial spectrum which shows a fringe separation of 0.2nm. This is converted

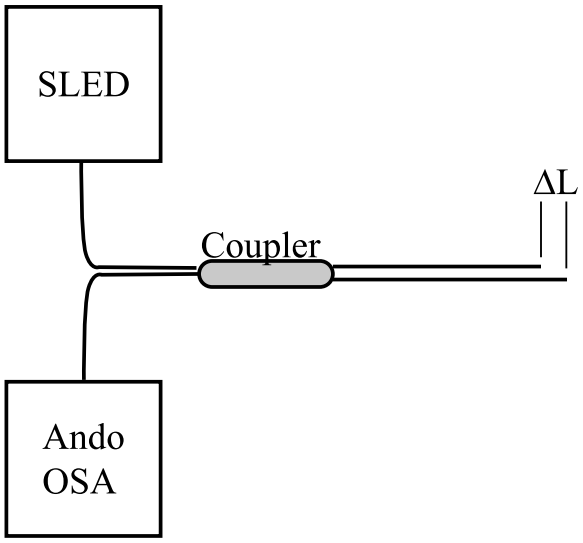

Figure 3.18. The fiber length difference is measured using a white light interferometer.

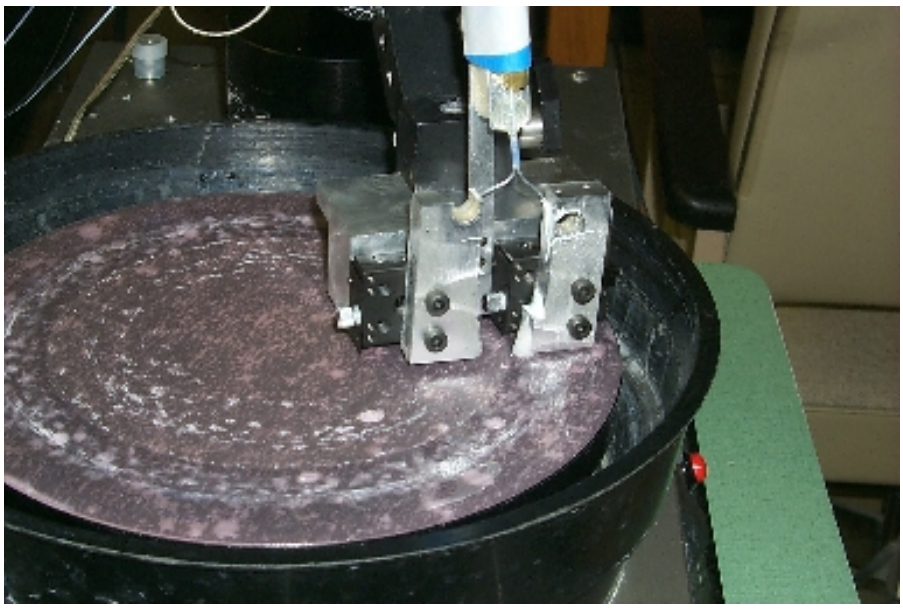

Figure 3.19. The fibers are mounted onto the polishing machine so that the pressure of each fiber against the lap can be controlled. Polishing continues until the desired length difference is achieved.

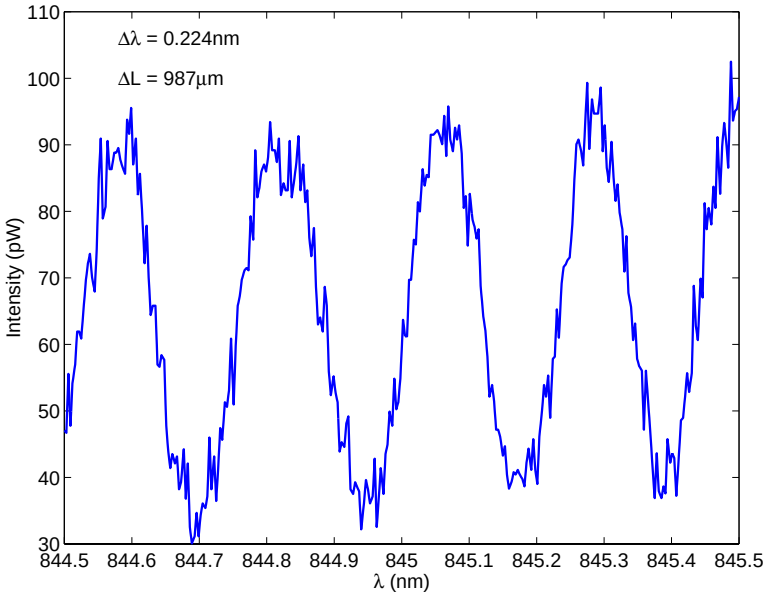

Figure 3.20. The initial spectrum obtained during the fringe generator manufacturing process which shows a fiber length difference of approximately 1mm.

to a fiber length difference using Equation (3.20). Doing so yields a length difference of approximately 1mm, which agreed with what we observed by pulling the two fibers taut. A spectrum mid-way through the polishing process is shown in Figure 3.21. The fringe separation has increased to approximately 1nm and the length difference decreased to 230μm.

The final spectrum we obtained using this system is shown by the red trace in Figure 3.22. The fringes readily observed in this trace give a fiber length difference of approximately 40μm. However, the blue trace in Figure 3.22 is a full width spectrum taken at the same time as Figure 3.20., when $\Delta L \approx$ 1mm. The actual fringes in this initial (blue) spectrum are of such high frequency they can barely be resolved. If we clean up the envelope of these spectra by running them through a low pass filter, as shown in Figure 3.23, we observe

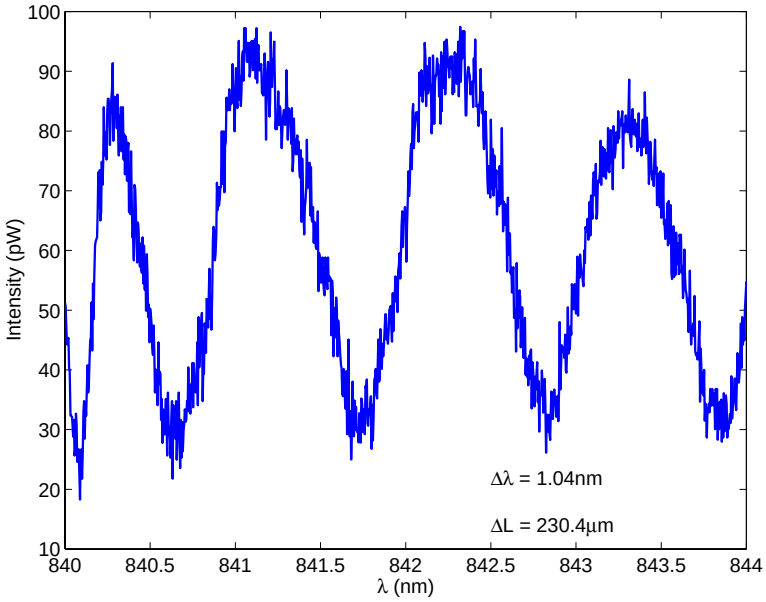

Figure 3.21. A spectrum mid–way through the process; the length difference has decreased to 230μm.

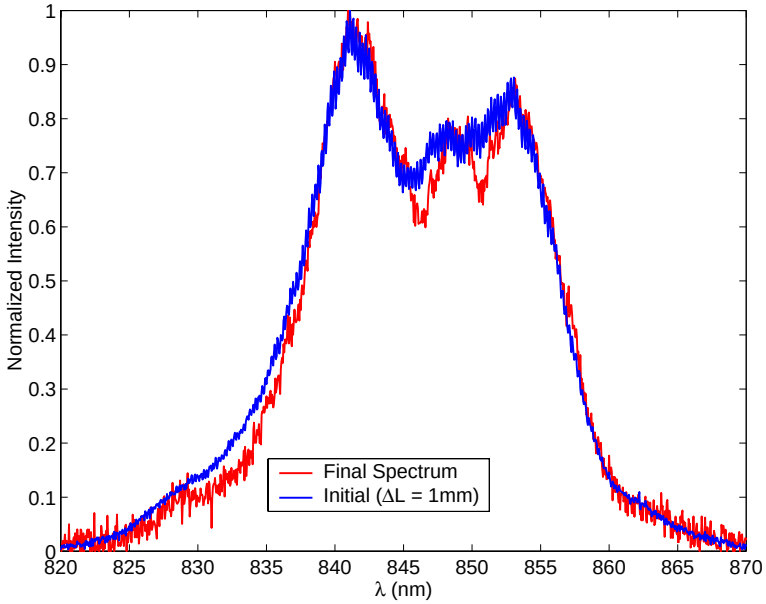

Figure 3.22. A comparison of the final spectrum (red) and initial spectrum (blue) taken at the same time as Figure 3.20. The fringes readily observed are noise arising from some other reflection in the system.

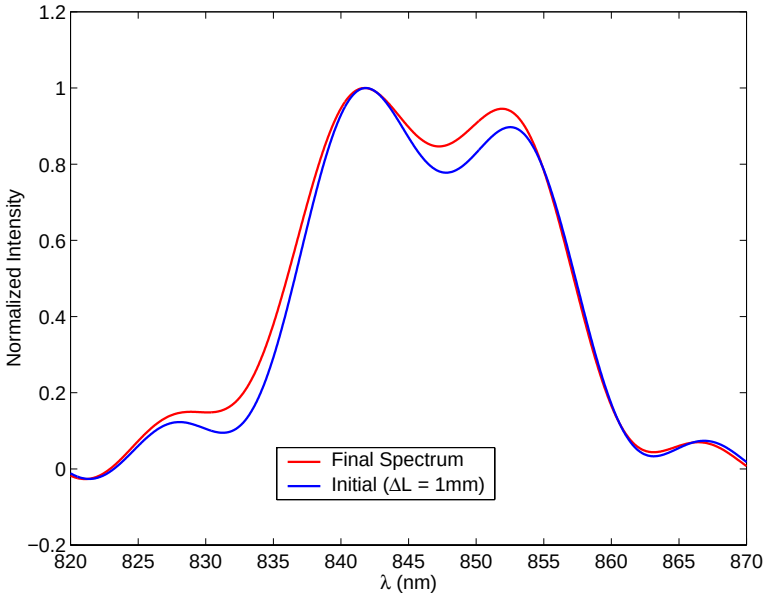

Figure 3.23. A low–pass filtered version of a spectra in Figure 3.22.

that they are almost identical. Hence, we conclude that the fringes observed in these spectra result from some other reflection in the system or modal noise in the SLED source. The "true" fringes resulting from the fiber endfaces have a period longer than the SLED spectrum width, which implies that the length difference is less than 6μm. Further, the amount the fiber was lowered during the polishing process was carefully recorded. These records correlated very well to spectra taken throughout the polishing process and also indicated a length difference less than 6μm.

Given the limitation of the SLED spectrum width, length differences smaller than 6μm could not reliably be measured. Hence continuing to polish the fibers would not be useful, especially since the length difference meets the requirement discussed at the beginning of Section 3.4. The length difference can now be compensated for by offsetting the fiber endfaces as depicted in Figure 3.6, without an excessive amount of dispersion induced phase shifting.

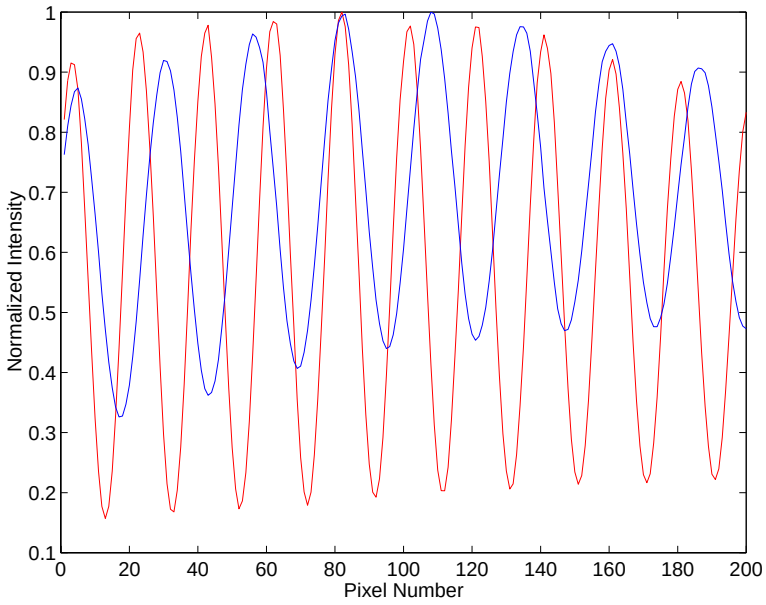

Figure 3.24. A cross section of the fringe pattern after the fibers were polished and aligned. The red trace is for the 633nm HeNe and the blue trace is for the 830nm laser diode. The zero order fringe is located pixel number 82.

3.4.4 Fiber Alignment and Calibration

After the polishing process was complete, the fibers were removed and each placed on a two-dimensional translation stage, which allowed the fiber separation and endface offset to be controlled. The fibers were aligned and the fringe pattern shown in Figure 3.24 was observed.

These results indicate that the fibers are properly aligned such that the zero order fringe, aligned with pixel number 82, does not move when the source wavelength is switched between the 633 and 830nm sources. The alignment of the two fibers was then fixed using standard epoxy.

Once the fibers were aligned, two calibration procedures were performed. The first

calibration determined the magnification of the camera at several z_o values within the measurement volume. The second calibration process determined the relationship between the phase of the fringe pattern and the height of the object.

In the first process, a grid of known spacing was placed onto a flat object and imaged by the camera at several locations. The distance between the grid lines was then measured (in units of pixels) and the camera's magnification determined. This magnification related the camera pixels to object dimension in meters. At $z_o = 0$, the magnification in the x_o direction was approximately 87μm per pixel, and 86μm per pixel in the y_o direction. For a standard 640 by 480 pixel camera, this yields a total viewing area of 55mm by 41mm.

Ideally, the second calibration process would not be necessary since Equation 3.11 can be used to relate object's height profile to the phase. In practice, however, Equation 3.11 possess too many degrees of freedom for calibration in a practical sense. Instead, an approach similar to presented by Saldner and Huntley [50] is used. In this process, the fringe pattern was projected onto a flat object at thirteen z_o locations within the measurement volume. The z_o values were evenly spaced in 2mm increments between $-12 \leq z_o \leq 12$. The phase was computed for each fringe pattern and the coefficients of a second order equation, a, b, and c were found using a least squares fit such that

$$z(m,n) = a(m,n) + b(m,n)\phi(m,n) + c(m,n)\phi^2(m,n). \tag{3.21}$$

Saldner and Huntley have shown that this method will result in errors less than 0.05%,

provided the maximum range of z_o values is less than 10% of the distance between the camera and the object. For our situation, this distance is 0.5m. Hence, the range of z_o must be less than 50mm.

A fiber optic Young's double pinhole interferometer has now been built, described, and modeled. We expect a resolution of approximately 0.1mm and a mapping volume of 55mm by 41mm by 26mm with a stand off distance of approximately one-half meter.

Chapter 4 Results and Discussion

Once the system was constructed and calibrated, several types of objects were profiled, a few of which are presented here. Items that will be presented include a flat glass plate with a 2mm step discontinuity, a metal cylinder (soda can), and a doll's face. All of the measured profiles correspond very well to the objects' actual profiles. The cylinder was used to measure the system's measurement accuracy over a large depth change (22mm) while the glass plate with the 2mm step was used to measure the systems resolution.

4.1 Reconstruction of a Doll's Face

Perhaps the most interesting result is the profile of the doll's face. A two dimensional picture of the doll is shown in Figure 4.1. This picture was taken with a Kodak digital camera. The surface of the doll's face was placed approximately one–half meter away from the pinholes and the camera and illuminated with fringes from both a HeNe laser and a 833nm laser diode. A sample of the fringe pattern from the HeNe source is shown in Figure 4.2

Using the fringe pattern in Figure 4.2, and the corresponding fringe pattern from the laser diode, the zero order fringe was determined, the phase of the fringe pattern was computed, and the surface was reconstructed. The reconstructed surface is shown in Figure 4.3(a).

Comparing Figures 4.1 and 4.3(a), we can clearly see the eye-socket, nose, mouth and

Figure 4.1. Picture of doll used as test object.

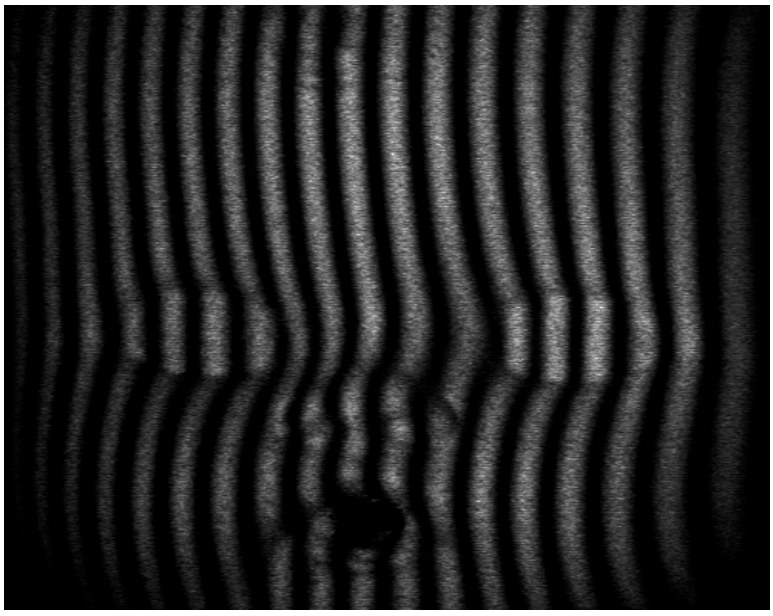

Figure 4.2. HeNe fringes on the doll's face.

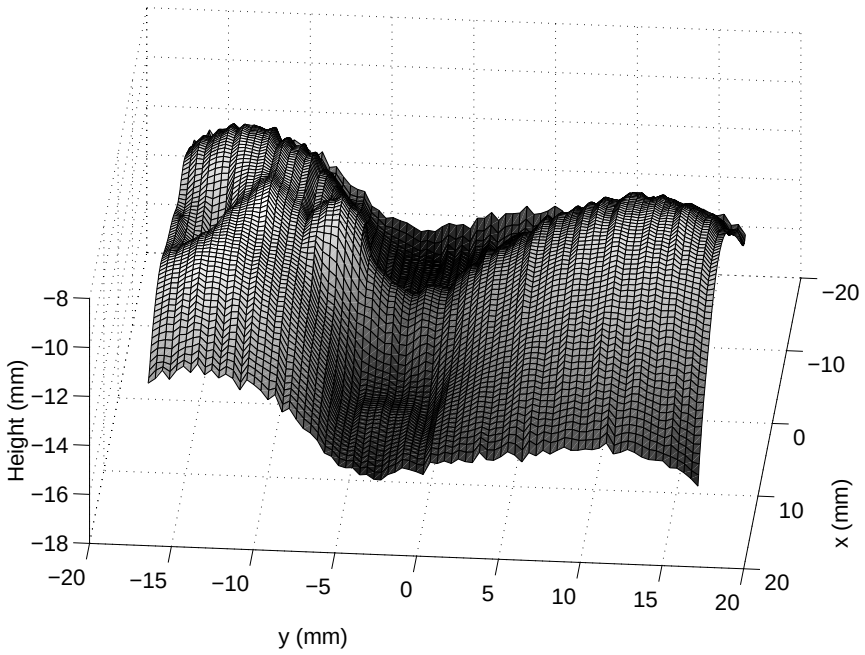

(a)

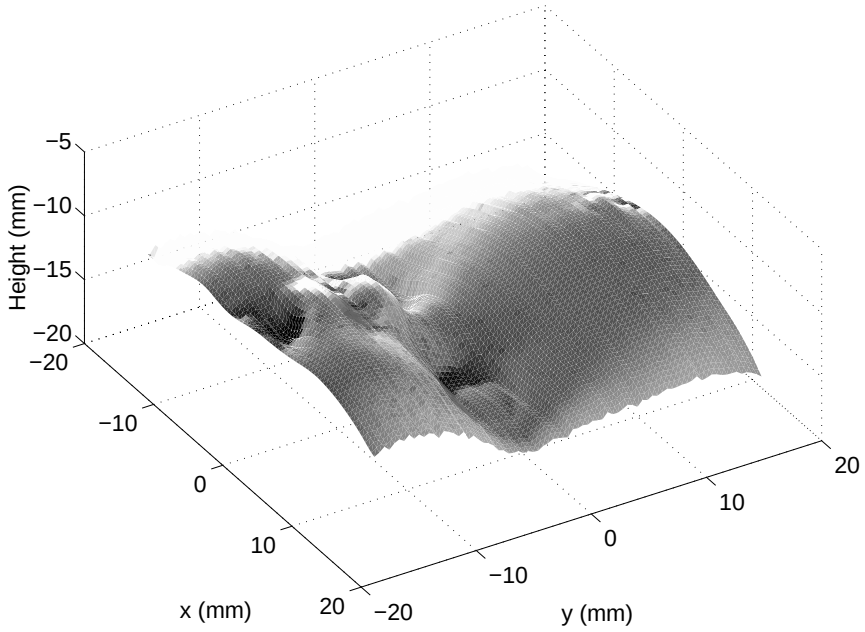

(b)

Figure 4.3. (a) Reconstructed surface of doll's face using the fringe pattern in Figure 4.2. Only every fifth data point is shown to improve the picture clarity. (b) Two–dimensional picture of the doll's face overlaid on top of the reconstructed surface which allows easier identification of the mouth, nose, and eye regions.

forehead. These details are easier to distinguish if a picture similar to Figure 4.1 is overlaid on top of the reconstructed surface, as shown in Figure 4.3(b). Here we can very clearly see that the various surface heights were accurately measured and reconstructed. It is also interesting to note that the doll's mouth, in which no fringes were visible, as seen in Figure 4.2, was still reconstructed as a recession, as seen in Figure 4.3.

4.2 Reconstruction of a Soda Can

Another object I profiled was the surface of a 12-ounce soda can. The reconstructed surface is shown in Figure 4.4(a), while the HeNe fringe pattern is shown in Figure 4.4(b). An interesting test of the system accuracy is to compare the measured surface with a circle of radius 33mm, which is the radius of the can measured with a set of calipers. This comparison is provided in Figure 4.5. The root mean squared error is computed to be 0.33mm. The root mean squared error is defined as:

$$\text{R.M.S.} = \sqrt{\left[\frac{1}{n}\sum_{1}^{n}(z_i - zt_i)^2\right]} \tag{4.1}$$

where z_i is the measured surface height and zt_i is the "true" surface height, defined as the height of the circle of radius 33mm. From Figure 4.5, the range of the surface height is approximately 22mm. Hence, the error is 1.5% of the measurement depth.

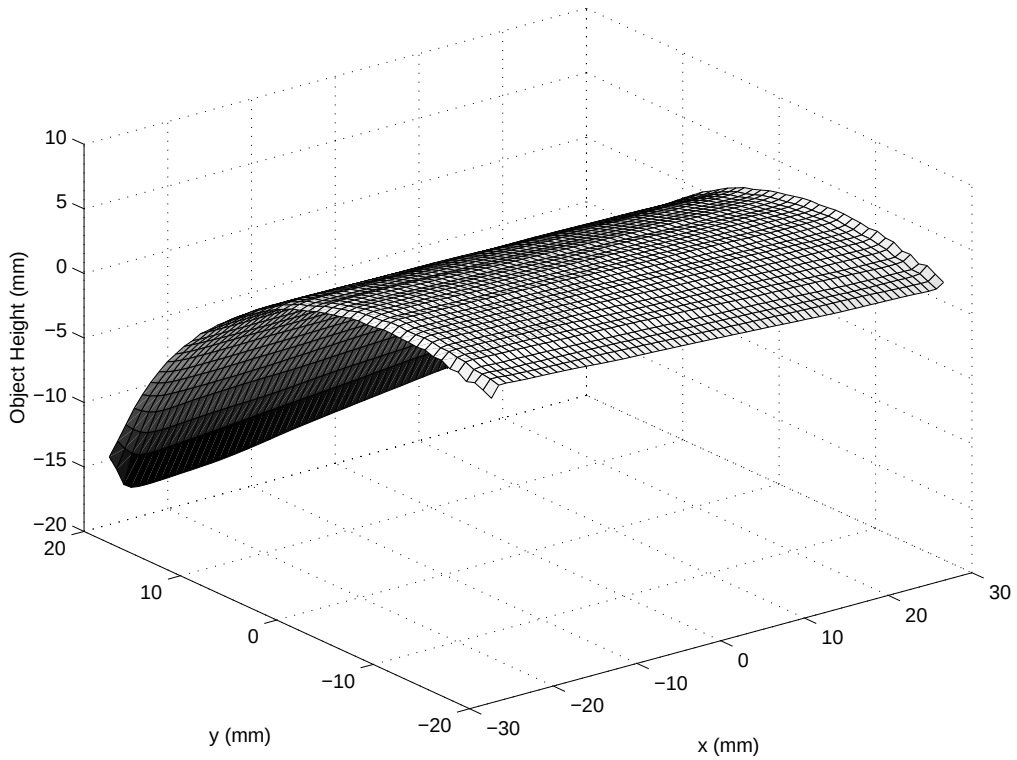

(a)

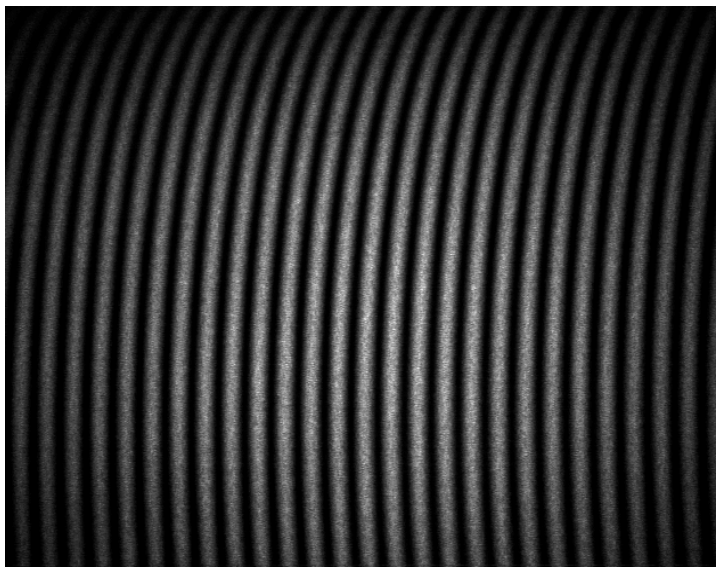

(b)

Figure 4.4. (a) Reconstructed surface of a soda can. (b) The HeNe fringe pattern from which (a) was reconstructed.

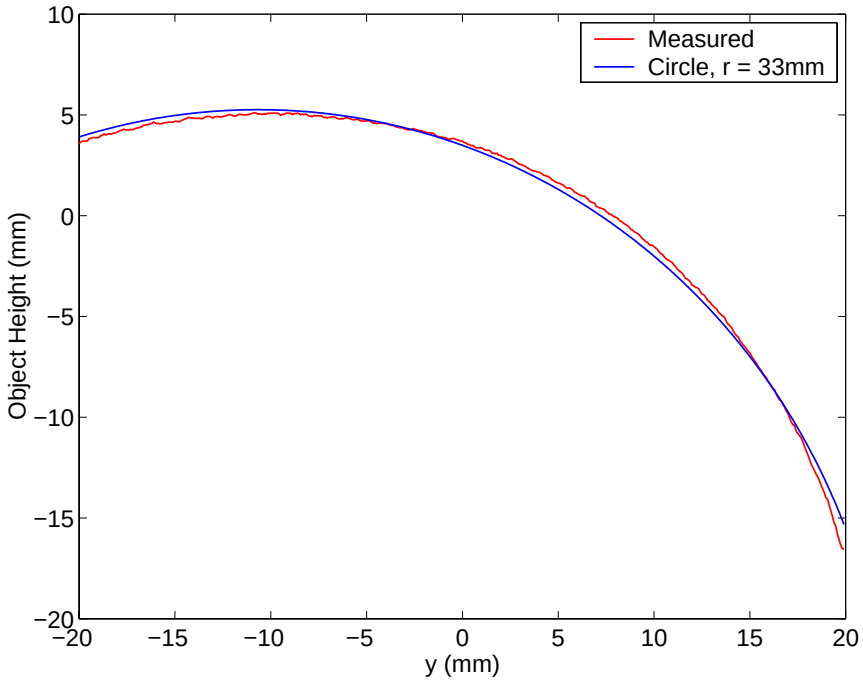

Figure 4.5. Comparison of a cross section of the can's surface in Figure 4.4(a) to a circle of radius 33mm. The R.M.S. error is 0.33mm.

4.3 Reconstruction of a Flat Plate and System Resolution

While perhaps a less interesting object to measure, the profiling and analysis of a flat plate with a step discontinuity can provide valuable insights into the resolution and accuracy of the system. A picture of the plate to be measured is shown in Figure 4.6(a). Examples of typical fringe patterns as projected onto the plate are shown in Figure 4.6(b) and (c).

Using these fringe patterns, the surface was profiled and plotted in Figure 4.7. From this plot, two things are readily noticeable. First, while the edge in the y_o direction appears to be sharp, the edge in the x_o direction is rounded. Also, ripples in the y_o direction appear

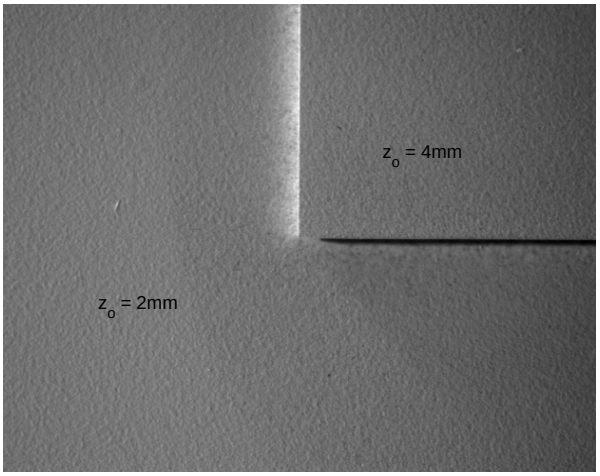

(a)

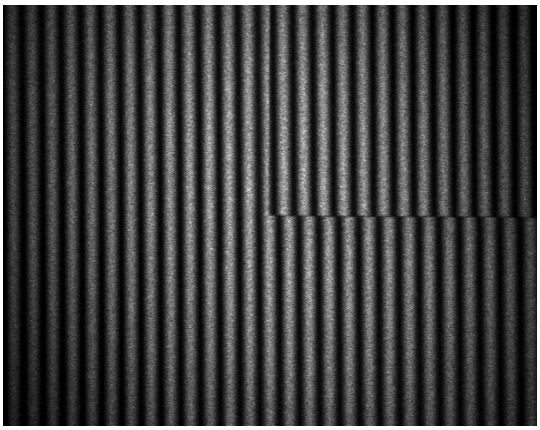

(b)

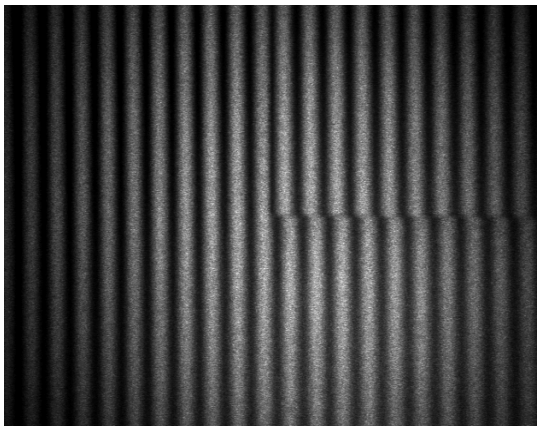

(c)

Figure 4.6. (a) Picture of a flat plate with a 2mm step. The area in the upper right–hand corner is 2mm higher than the rest of the plate. (b) A typical HeNe fringe pattern on the plate. (c) A typical Laser Diode (833nm) fringe pattern.

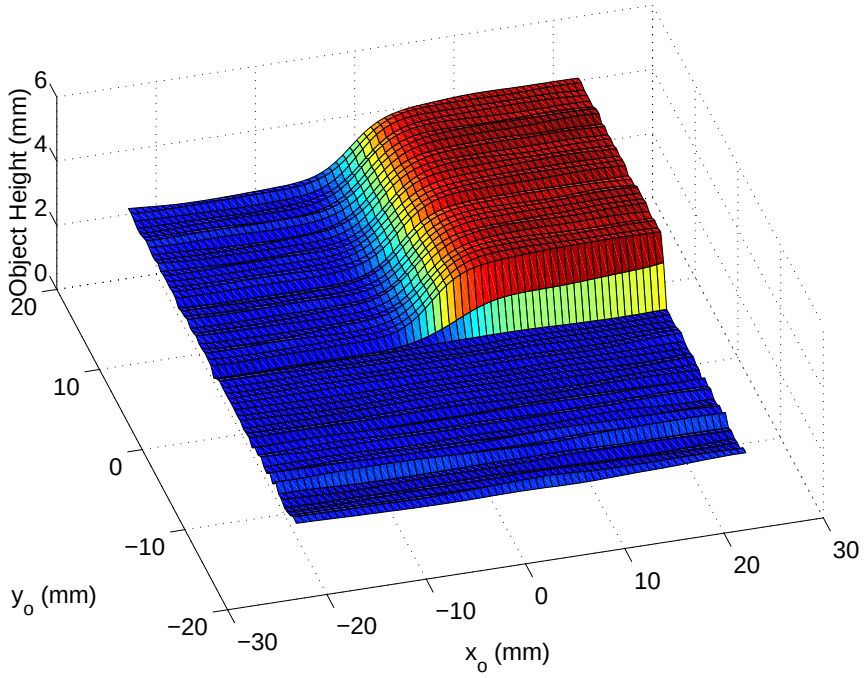

Figure 4.7. The reconstructed surface of the object in Figure 4.6(a).

on the surface. Both of these effects are more easily seen by plotting a cross–section in both the x_o and y_o directions, as shown in Figure 4.8.

The smoothed edge in the x_o direction and the sharp edge in the y_o direction is a byproduct of the phase detection method. Recall from Section 2.2.2 that the phase is detected by taking the Fourier transform in the x_o direction, band–pass filtering the spectrum, and then taking the inverse Fourier transform. This filtering process is done by multiplying the spectrum by a Gaussian function, centered on the "carrier" frequency of the fringes, as illustrated in Figure 3.4(b). Since multiplication in the frequency domain is convolution in the space domain [15], we are not surprised by the smoothing in the x_o direction. No Fourier transform operation or band–pass filtering is done in the y_o direction, hence, the

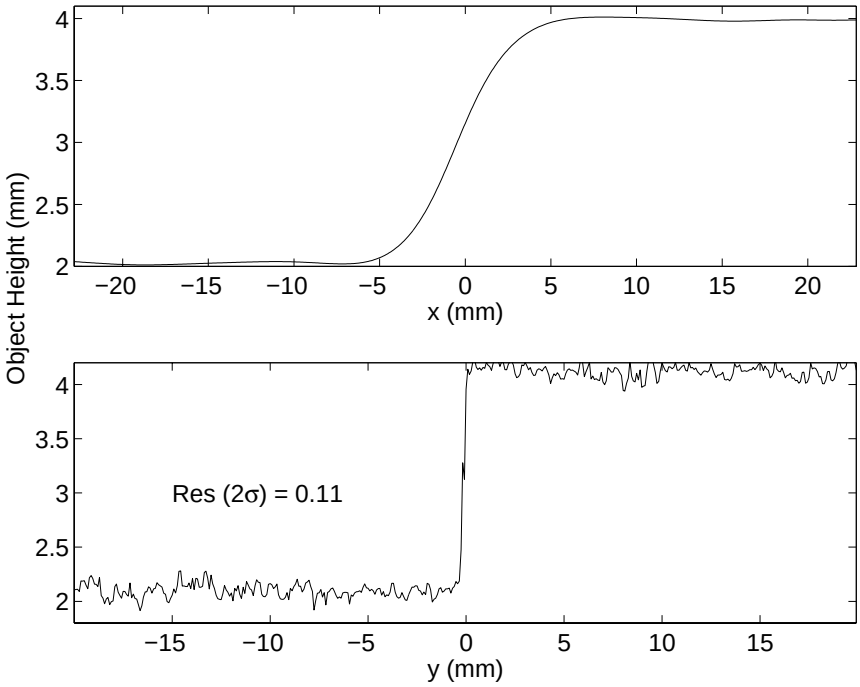

Figure 4.8. Cross–section of the reconstructed surface shown in Figure 4.7. The top graph is in the x_o direction and the lower graph in the y_o direction. From the lower plot, the resolution of the system is estimated as 0.11mm, which is twice the standard deviation of the measurements.

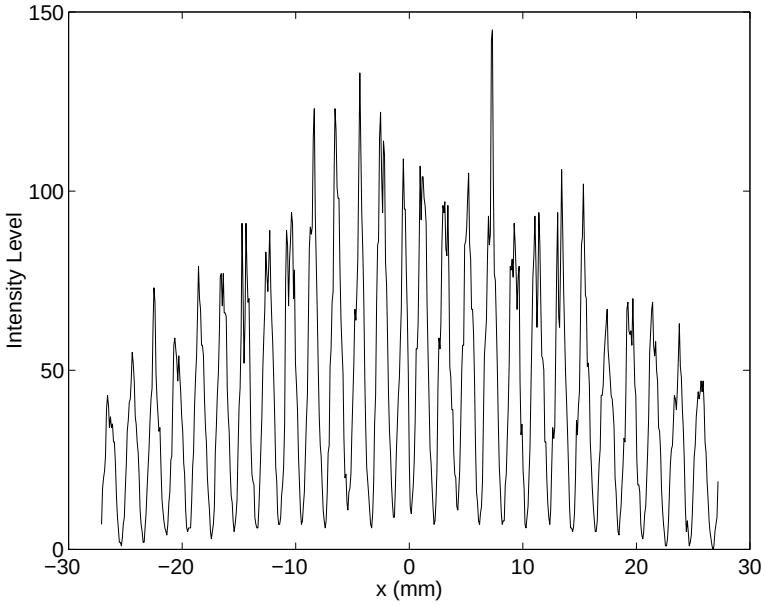

Figure 4.9. A representative raw HeNe fringe pattern. There are approximately 100 intensity levels between the peaks and valleys of the fringe pattern, as assumed when the system resolution was estimated in Section 3.3.1.

edge remains sharp as seen in the bottom plot of Figure 4.8.

In the y_o direction, the ripples on the surface limit the depth resolution of the system. Using the standard definition that resolution is twice the standard deviation, we conclude that the resolution of the system is 0.11mm. This corresponds very well to the estimated amount in Figure 3.5 for a viewing angle of 14 degrees. These estimates were based on an expected number of intensity (gray) levels between the peak and valleys of the fringe pattern of 100, which is very close to what was actually observed, as shown in Figure 4.9. If the number of intensity levels were increased (*i.e.* if the signal–to–noise ratio were improved) then we would expect the system resolution to improve, as predicted by Equation 3.12. An interesting comparison is to examine the relationship between the variations of the measured surface height of a flat object and the centroid of the zero–order fringe. Since the object is flat,

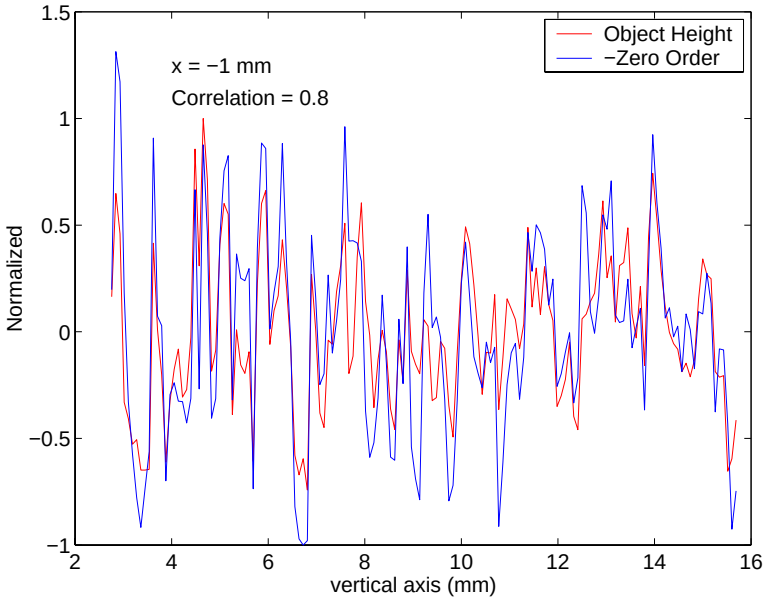

Figure 4.10. The variations of the surface height are closely correlated to the variations of the calculated centroid of the zero order fringe. The normalized object height is shown in red, while the negative of the normalized zero order fringe centroid is shown in blue. These two effects are strongly correlated with correlation coefficient of 0.8.

we would expect the zero–order fringe to be perfectly straight with any variations resulting from noise in the system. This comparison is shown in Figure 4.10, where the negative of the zero order fringe is actually shown since if the fringe moves to the left (negative), the calculated surface height increases. We can easily see the strong correlation between the zero–order fringe centroid and the surface height variations. The correlation coefficient is computed to be 0.8.

Figure 4.10 is a plot along the y_o direction at $x_o = -1$mm. For this data set, the zero order fringe was located at approximately 1.5mm. If we compute the correlation coefficient along the y_o direction for every x_o value, we get the plot shown in Figure 4.11. The vertical line is located at the average value of the zero order fringe centroid ($x_o \approx 1.5$mm). Note

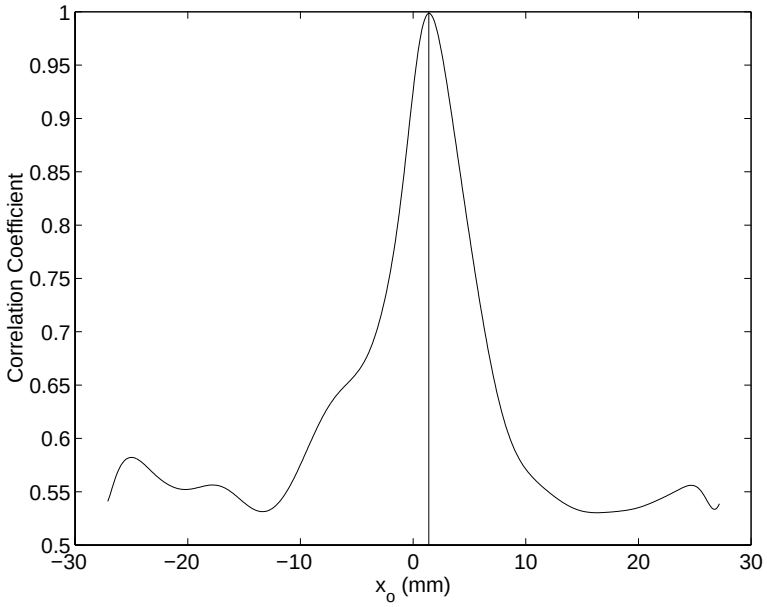

Figure 4.11. Correlation coefficient between surface height variations and zero–order centroid variations for a flat object for every x_o value. The vertical line is located at the average centroid location.

that the correlation peaks at this location and falls off away from this point.

This is interesting primarily because it relates to the system resolution predicted in Section 3.3.1 and observed previously in this section. If the SNR were improved, it is natural to assume that our calculation of the zero–order fringe centroid would also improve. Given the strong correlation between the centroid variations and surface height variations in Figure 4.10, we can assume that the resolution would also improve, just as predicted by Equation 3.12.

Note that the measured step height from Figure 4.8 was 2.02mm. This corresponds extremely well to the "true" step height of 2.0mm, as measured by a pair of micrometers. This would yield an error of less than 1% of the measurement depth.

The time required to compute the surface map, once the images of the fringe pattern are captured and loaded into the computer, is less than 5 seconds on a 500MHz Pentium III computer.

From the results presented in this section, we can conclude that the system can accurately measure and reconstruct both simple and complex surfaces, such as the doll's face. The system resolution was measured to be 0.11mm, which agrees with the estimated values in Section 3.3. It is believed that this resolution would improve if the signal to noise ratio were improved. The R.M.S. error of the system was measured to be less than 1.5% of the measurement depth.

Chapter 5 Conclusions

This research presented a novel method of constructing a non–contact surface profilometer using a Young's double pinhole interferometer. The interferometer was constructed by using a single mode fiber optic two by two coupler. The lengths of the output fibers were carefully controlled so as to ensure the phases at the output were nearly identically. The fibers were aligned side–by–side to form the "pinholes." Once constructed and aligned, two wavelengths are sequentially projected through the fibers so that the zero–order fringe can be determined. The zero order fringe will be in the same location at both wavelengths. The phase of the fringe pattern is then calculated using the Fourier transform fringe analysis technique and the phases are unwrapped from their modulo 2π values using the information from the zero–order fringe. The system has a depth resolution (2σ) of approximately 0.1mm. This agrees very well with the predicted value based on the viewing angle. This resolution could be improved if the power reflected from the object were increased. The measurement error of the system (measured surface height versus true surface height) was less than 1.5% of the maximum surface depth. Further, the surface map computation took less than 5 seconds on a Pentium III computer.

There are several advantages and novelties in this system versus other methods of performing 3–D mapping. First, the use of a fiber optic coupler as the fringe projector greatly reduces the size and weight of the system, which could prove to be very useful in space constrained applications such as mounting the system on a robotic arm. While the use of

fiber optics to form a Young's interferometer is not entirely new, all other systems to my knowledge use post–coupler fiber lengths of a meter or more. In the system developed in this research, the leads were cut short to reduce the effects of vibration and thermal drift on the output phase. This greatly improved the stability of the fringes on the object. Further, fiber optics allows the laser sources to be located meters away. While this also reduces the weight of the system, its greatest advantage is in applications where heat management is critical.

The size and weight of the system was further reduced over other 3–D mapping systems by not using optics to collimate the fringe pattern. While this increased the complexity of the reconstruction equations, the only bulk optics are those associated with the objective lens on the camera. This reduction in the number of critically aligned optics will decrease the cost of the system.

Another novelty over other 3–D mapping systems is the use of the zero–order fringe as a calibration line in the phase unwrapping process. This allows the absolute phase to be measured, alleviates phase unwrapping problems associate with step discontinuities in the object profile, and increases the dynamic range of the system. Step discontinuities are commonly encountered when measuring real objects. Many researchers in this field believe that phase unwrapping is the most challenging aspect of optical profilometry. To use the zero–order fringe, the lengths of the post–coupler fiber had to be precisely controlled. To accomplish this, an approach was developed which used a white–light–interferometer to measure and polish the fibers to within 6μm of each other.

In summary, the non–contact profilometer developed during this research increases the

applications that can be served by 3–D mapping. Precisely controlling the fiber lengths and using dual wavelengths to determine the zero order fringe provides another means by which the phase of the fringe pattern can be accurately unwrapped, even with step discontinuities on the objects surface.

Appendix A Detailed Analysis of Optimum Viewing Angle

Taking the derivative of Equation 3.11 with respect to ϕ, we obtain

$$\begin{aligned}\frac{\mathrm{d}z_o}{\mathrm{d}\phi} &= \frac{[\cos\beta\sin\beta]\left[2akx_o\cos\beta\sin\beta-\phi\left(L\cos\beta+x_o\sin^2\beta\right)\right]}{\left(\phi\cos\beta\sin\beta+k2a\sin^2\beta\right)^2} \\ &\quad +\frac{L\cos\beta+x_o\sin^2\beta}{\phi\cos\beta\sin\beta+k2a\sin^2\beta}.\end{aligned} \tag{A.1}$$

Note that we have dropped the (m,n) dependence on ϕ, and x_o for convenience. This expression has many dependencies, including the location along the object (x_o) and the phase (ϕ) which includes the shape of the object. To proceed, we need to define the object so that these dependencies can be combined. It is convenient to define the object to be a flat surface perpendicular to the fiber axis – that is the (x_p, z_p) plane from Figure A.1. This is equivalent to saying that $y_p = 0$. Since we know that $x_o = x_p\sin\beta + y_p\cos\beta$, then $x_o = x_p\sin\beta$. Also from Figure A.1, x_p can be defined as $x_p = d\tan\theta$. Combining these relationships gives us $x_o = d\tan\theta\sin\beta$. Equation A.1 can now be simplified to

$$\begin{aligned}\frac{\mathrm{d}z_o}{\mathrm{d}\phi} &= \frac{2akd\tan\theta\sin\beta\cos^2\beta-\phi\left(d\cos\beta-d\tan\theta\sin^2\beta\cos\beta\right)}{\left(\phi\cos\beta+k2a\sin\beta\right)^2} \\ &\quad +\frac{d\left(1+\tan\theta\sin^2\beta\right)}{\phi\cos\beta+k2a\sin\beta}.\end{aligned} \tag{A.2}$$

Since the object's surface has been defined, the phase can now be determined as function of θ. Using Equation 3.1, and the above relationship for x_p,

$$\phi = \frac{2a}{d} k x_p = 2ak \tan\theta. \tag{A.3}$$

Note that if we assume $\theta = 0$, and use Equation 3.5, then Equation A.2 reduces to the collimated fringes result presented in Section 3.3.1. In Equation A.2, there are three variables: the viewing angle, β, the distance to the object, d, and the illumination angle, θ. All other terms are constants or functions of these three variables.

To analyze this expression, we have presented several plots in Figure A.2, where we calculated the minimum detectable height, or the system resolution. Note the similarities to Figure 3.5. Once again, we have assumed that the minimum detectable phase difference is $2\pi/100$, based on a camera with 256 gray levels. The four plots in Figure A.2 correspond to four different locations along the object defined by $\theta/\theta_{\max} = 0, 1/3, 2/3, \text{and } 1$. The maximum angular value of the fringe pattern, defined by the fiber's acceptance angle, is denoted as $\theta_{\max} = \sin^{-1}(\text{NA})$, where NA is the numerical aperture of the fiber.

Note that as the position moves to the right (towards larger values of $\theta/\theta_{\max}$), the resolution improves. This is due to a decrease in the size of the camera pixels imaged onto the object. Recall that we assumed the object was a flat surface defined by $y_p = 0$. Hence, this surface is not parallel to the camera's CCD surface. As we move towards larger values of $\theta/\theta_{\max}$, the pixel size gets smaller as illustrated in Figure A.3. Smaller pixels on the

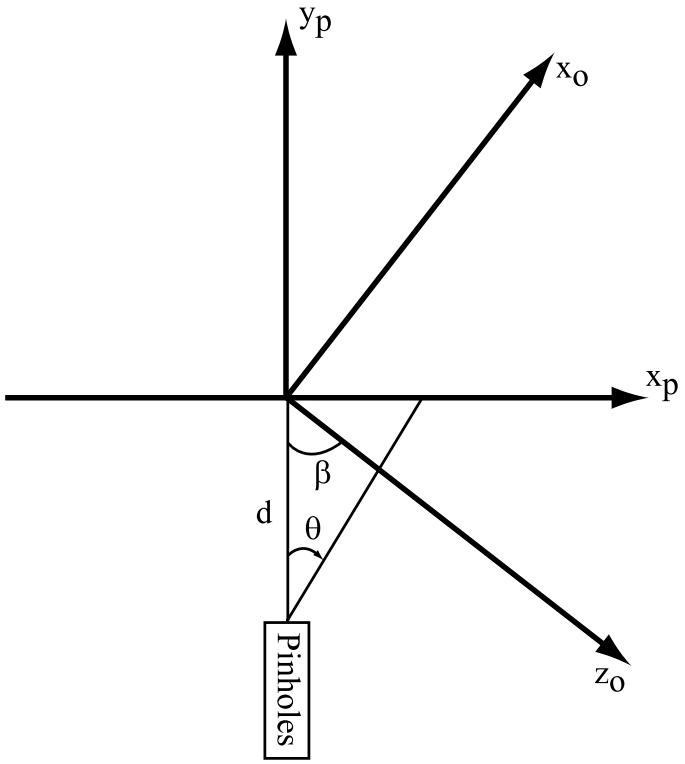

Figure A.1. Coordinate Systems used for analysis of system resolution. β is the angle between the pinhole (fiber) axis and the camera axis, also called the viewing angle. θ is the angle between the pinhole axis and a point x_p axis, also called the illumination angle.

surface translate to a higher resolution. Conversely, as the illumination point moves towards the left (negative values of $\theta/\theta_{\max}$), the resolution degrades.

Despite these fluctuations, the general shape as a function of the viewing angle, β, stays relatively constant and our decision to design towards a viewing angle of 10 to 15 degrees is not affected.

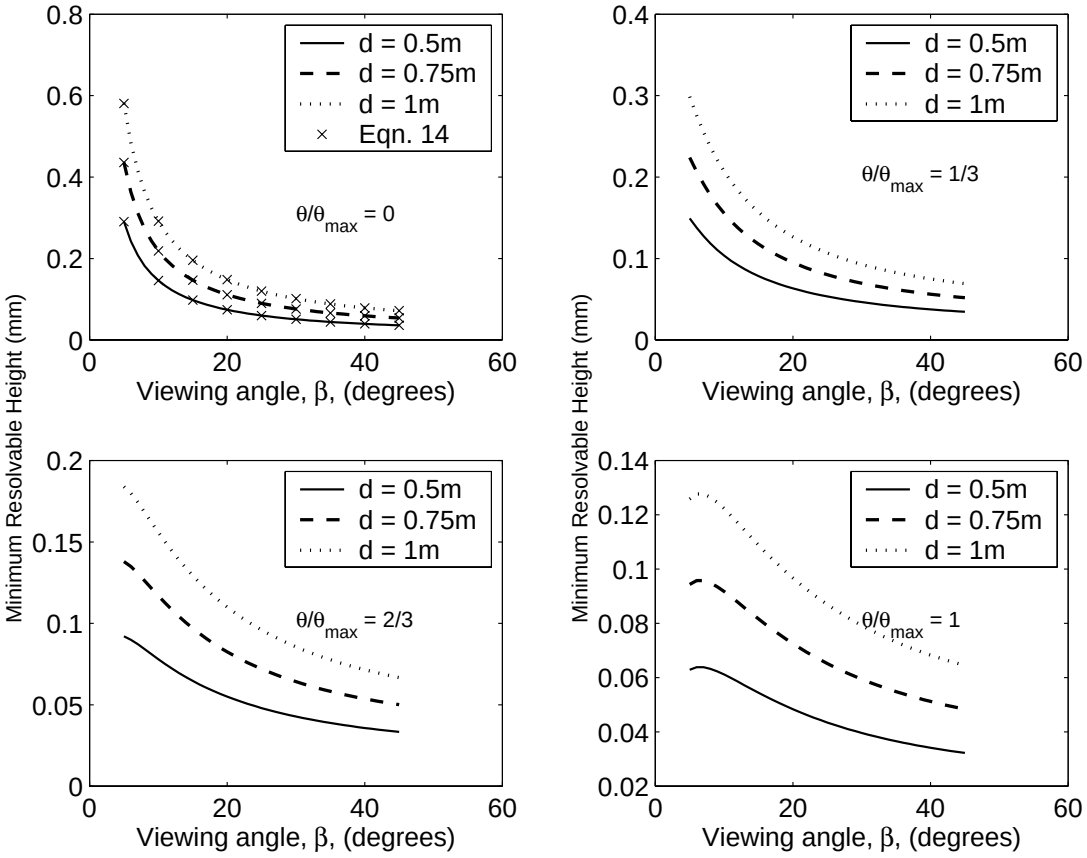

Figure A.2. The predicted system resolution based Equation 3.11. The top left plot is for $\theta/\theta_{\max} = 0$, which corresponds to the zero order fringe. These results are identical to those obtained using the simplified equation, as indicated by the "x's.". The remaining plots are for points along the object, one–third and two–thirds the distance from the center to the edge of the distribution and at the edge of the distribution.

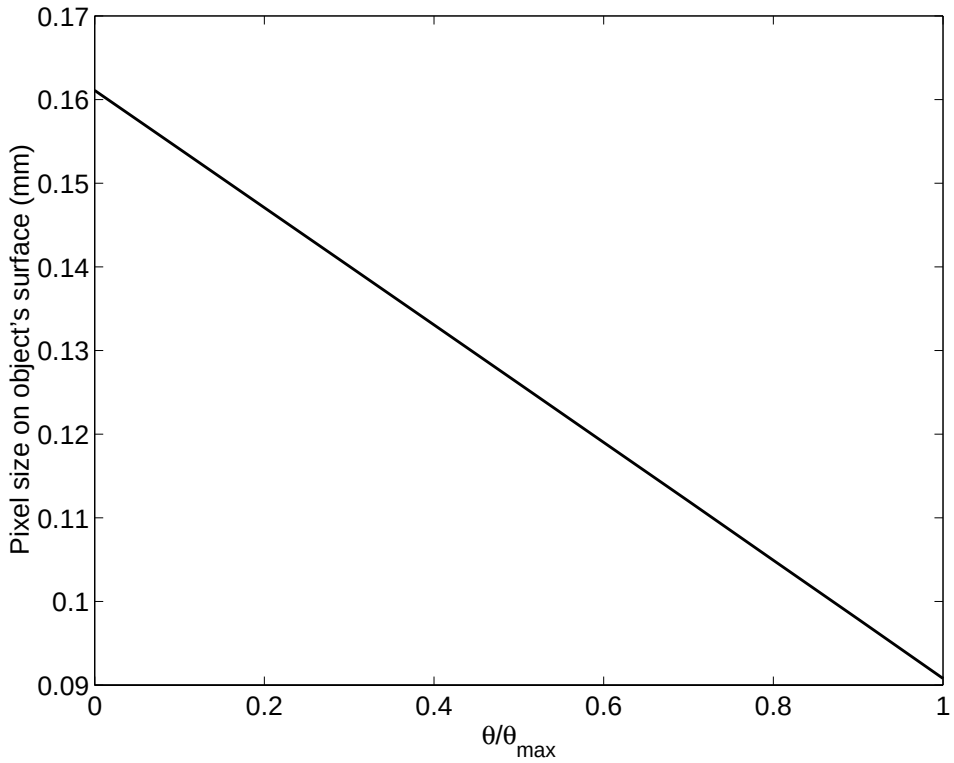

Figure A.3. The size of the camera pixels as a function of the normalized illumination angle, $\theta/\theta_{\max}$. This is calculated based on a focal length of 38mm and a mean object distance of $d = 0.75$m.

Bibliography

[1] M. J. Adams. *An Introduction to Optical Waveguides*. John Wiley and Sons, New York, 1981.

[2] Yasuhiko Aral, Isao Ishihara, and Shunsuke Yokozeki. Automatic spatial fringe analysis method for two–dimensional fringes image including phase discontinuities by obstructions. *Journal of Modern Optics*, 45(10):2011–2023, 1998.

[3] Donald J. Bone. Fourier fringe analysis: The two–dimensional phase unwrapping problem. *Applied Optics*, 30(25):3627–3631, 1 September 1991.

[4] J.H. Bruning, D.R. Herriott, J.E. Gallagher, D.P. Rosenfeld, A.D. White, and D.J. Brangaccio. Digital wavefront measuring interferometer for testing optical surfaces and lenses. *Applied Optics*, 13(11):2693–2703, November 1974.

[5] David R. Burton, Anthony J. Goodall, John T. Atkinson, and Michael J. Lalor. The use of carrier frequency shifting for the elimination of phase discontinuities in fourier transform profilometry. *Optics and Lasers in Engineering*, 23(4):245–257, 1995.

[6] David R. Burton and Michael J. Lalor. Multichannel Fourier fringe analysis as an aid to automatic phase unwrapping. *Applied Optics*, 33(14):2939–2948, 10 May 1994.

[7] Paul G. Charette and Ian W. Hunter. Robust phase–unwrapping method for phase images with high noise content. *Applied Optics*, 35(19):3506–3513, 1 July 1996.

[8] Frank Chen, Gordon M. Brown, and Mumin Song. Overview of three–dimensional shape measurement using optical methods. *Optical Engineering*, 39(1):10–22, January 2000.

[9] Wenjing Chen, Hu Yang, Xianyu Su, and Songxin Tan. Error caused by sampling in Fourier transform profilometry. *Optical Engineering*, 38(6):1029–1034, June 1999.

[10] Katherine Creath. Step height measurement using two–wavelength phase–shifting interferometry. *Applied Optics*, 26(14):2810–2816, 15 July 1987.

[11] Katherine Creath. Phase–measurement interferometry techniques. In E. Wolf, editor, *Progress in Optics*, volume 26, pages 350–393. Elsevier Science Publishers, 1988.

[12] Katherine Creath. Temporal phase measurement methods. In David W. Robinson and Graeme T. Reid, editors, *Interferogram Analysis, Digital Fringe Pattern Measurement Techniques*, chapter 4, pages 94–140. Institute of Physics Publishing, Bristol, 1993.

[13] Peter de Groot. Derivation of algorithms for phase–shifting interferometry using the concept of a data–sampling window. *Applied Optics*, 34(22):4723–4730, 1 August 1995.

[14] W. G. Driscoll, editor. *Optical Society of America: Handbook of Optics*. McGraw–Hill, New York, 1978.

[15] Jack D. Gaskill. *Linear Systems, Fourier Transforms, and Optics*. John Wiley and Sons, New York, 1978.

[16] Dennis C. Ghiglia, Gary A. Mastin, and Louis A. Romero. Cellular–automata method for phase unwrapping. *Journal of the Optical Society of America A*, 4(1):267–280, January 1987.

[17] Jeffrey J. Gierloff. Phase unwrapping by regions. In *Proceedings of the SPIE: Current Developments in Optical Engineering II*, volume 818, pages 2–9, 1987.

[18] Joseph W. Goodman. *Introduction to Fourier Optics*. McGraw-Hill Publishing Company, New York, 1968.

[19] Miguel Arevalillo Herraez, David R. Burton, Michael J. Lalor, and David B. Clegg. Robust, simple, and fast algorithm for phase unwrapping. *Applied Optics*, 35(29):5847–5852, 10 October 1996.

[20] Cheng Ho et al. Demonstration of literal three–dimensional imaging. *Applied Optics*, 38(9):1833–1840, 20 March 1999.

[21] Kai Man Hung and T. Yamada. Phase unwrapping by regions using least–squares approach. *Optical Engineering*, 37(11):2965–2970, November 1998.

[22] Jonathan M. Huntley. Automated fringe pattern analysis in experimental mechanics: A review. *Journal of Strain Analysis*, 33(2):105–125, 1998.

[23] Jonathan M. Huntley and Henrik O. Saldner. Temporal phase-unwrapping algorithm for automated interferogram analysis. *Applied Optics*, 32(17):3047–3052, 10 June 1993.

[24] Jonathan M. Huntley and Henrik O. Saldner. Error–reduction methods for shape measurement by temporal phase unwrapping. *Journal of the Optical Society of America A*, 14(12):3188–3195, December 1997.

[25] Jonathan M. Huntley and Henrik O. Saldner. Shape measurement by temporal phase unwrapping: Comparison of unwrapping algorithms. *Measurement and Science Technology*, 8:986–992, 1997.

[26] G. Indebetouw. Profile measurement using projection of running fringes. *Applied Optics*, 17(18):2930–2933, September 1978. Reprinted in *Selected Papers on Optical Moire and Applications*, SPIE Milestone Series, Guy Indebetouw and Robert Czarnek editors, SPIE Optical Engineering Press, Bellingham, Washington, 1992.

[27] G. Indebetouw. A simple optical noncontact profilometer. *Optical Engineering*, 18(1):63–66, January 1979.

[28] Guy Indebetouw and Robert Czarnek, editors. *Selected Papers on Optical Moire and Applications*. SPIE Milestone Series. SPIE Optical Engineering Press, Bellingham, Washington, 1992.

[29] Yukihiro Ishii, Jun Chen, and Kazumi Murata. Digital phase–measuring interferometry with a tunable laser diode. *Optics Letters*, 12(4):233–235, April 1987.

[30] Kazuyoshi Itoh. Analysis of the phase unwrapping algorithm. *Applied Optics*, 21(14):2470, 15 July 1982. letter.

[31] Ramesh Jain, Rongachar Kasturi, and Brian Schunck. *Machine Vision*. McGraw–Hill, Inc., New York, 1995.

[32] Thomas R. Judge and Peter J. Bryanston-Cross. A review of phase unwrapping techniques in fringe analysis. *Optics and Lasers in Engineering*, 21:199–239, 1994.

[33] Thomas R. Judge, Chenggen Quan, and Peter J. Bryanston-Cross. Holographic deformation measurements by Fourier transform technique with automatic phase unwrapping. *Optical Engineering*, 31(3):533–543, March 1992.

[34] D. Kerr, G. H. Kaufmann, and G. E. Galizzi. Unwrapping of interferometric phase–fringe maps by the discrete cosine transform. *Applied Optics*, 35(5):810–816, 10 February 1996.

[35] W. D. Kingery, H. K. Bowen, and D. R. Uhlmann. *Introduction to Ceramics*. John Wiley and Sons, New York, 2nd edition, 1976.

[36] Malgorzata Kujawinska. Spatial phase measurement methods. In David W. Robinson and Graeme T. Reid, editors, *Interferogram Analysis, Digital Fringe Pattern Measurement Techniques*, chapter 5, pages 141–193. Institute of Physics Publishing, Bristol, 1993.

[37] Jie-Lin Li, Hong-Jun Su, and Xian-Yu Su. Two–frequency grating used in phase–measuring profilometry. *Applied Optics*, 36(1):277–280, January 1997.

[38] Tianchu Li, Anbo Wang, Kent Murphy, and Richard Claus. White–light scanning fiber Michelson interferometer for absolute position–distance measurement. *Optics Letters*, 20(7):785–787, 1 April 1995.

[39] Ming Luo. Optical analysis and opto–mechanical design for miniaturized laser illumination module in 3D areal mapper. Master's thesis, Virginia Polytechnic Institute and State University, Blacksburg, VA, April 2000.

[40] Daniel Malacara, Manuel Servin, and Zacarias Malacara. *Interferogram Analysis for Optical Testing*. Marcel Dekker, Inc., New York, 1998.

[41] Dietrich Marcuse. *Theory of Dielectric Optical Waveguides*. Academic Press, San Diego, second edition, 1991.

[42] Jose L. Marroquin, Maximino Tapia, Ramon Rodreguez-Vera, and Manuel Servin. Parallel algorithms for phase unwrapping based on Markov random field models. *Journal of the Optical Society of America A*, 12:2578–2585, December 1995.

[43] Alan V. Oppenheim and Ronald W. Schafer. *Discrete–Time Signal Processing*. Prentice Hall, Englewood Cliffs, New Jersey, 1989.

[44] Timothy L. Pennington, Anbo Wang, Hai Xiao, and Russell May. Manufacturing of a fiber optic Youngs double pinhole interferometer for use as a 3–D profilometer. *Optics Express*, 6(10):196–201, 8 May 2000. *www.opticsexpress.org*.

[45] C. Quan, H. M. Shang, C. J. Tay, and P. J. Bryanston-Cross. Holographic contouring using double–source technique and Fourier transform analysis. *Optics and Lasers in Engineering*, 30:351–362, 1998.

[46] G. T. Reid. Automatic fringe pattern analysis: A review. *Optics and Lasers in Engineering*, 7:37–68, 1986/87.

[47] Marc Rioux. Laser range finder based on synchronized scanners. *Applied Optics*, 23(21):3837–3844, 1 November 1984.

[48] David W. Robinson. Phase unwrapping methods. In David W. Robinson and Graeme T. Reid, editors, *Interferogram Analysis, Digital Fringe Pattern Measurement Techniques*, chapter 6, pages 194–229. Institute of Physics Publishing, Bristol, 1993.

[49] S. H. Rowe and W. T. Welford. Surface topography of non–optical surfaces by projected interference fringes. *Nature*, 216:786–787, November 1967.

[50] Henrik O. Saldner and Jonathan M. Huntley. Profilometry using temporal phase unwrapping and a spatial light modulator-based fringe projector. *Optical Engineering*, 36(2):610–615, February 1997.

[51] Henrik O. Saldner and Jonathan M. Huntley. Shape measurement of discontinuous objects using projected fringes and temporal phase unwrapping. In *Proceedings of the International Conference on Recent Advances in 3–D Digital Imaging and Modeling.*, pages 44–50. National Research Council Canada, IEEE, 12-15 May 1997.

[52] Henrik O. Saldner and Jonathan M. Huntley. Temporal phase unwrapping: application to surface profiling of discontinuous objects. *Applied Optics*, 36(13):2770–2775, 1 May 1997.

[53] Bahaa E. A. Saleh and Malvin Carl Teich. *Fundamentals of Photonics*. John Wiley and Sons, New York, 1991.

[54] D.G. Sandler, L. Cuellar, M. Lefebvre, T. Barrett, R. Arnold, P. Johnson, A. Rego, G. Smith, G. Taylor, and B Spivey. Shearing interferometry for laser–guide–star atmospheric correction at large d/r_o. *Journal of the Optical Society of America, A*, 11(2):858–873, February 1994.

[55] Giovanna Sansoni, Luca Biancardio, Umberto Minoni, and Franco Docchio. A novel, adaptive system for 3–D optical profilometry using a liquid crystal ligth projector. *IEEE Transaction on Instumentation and Measurement*, 43(4):558–566, August 1994.

[56] M. Servin, J. L. Marroquin, and F. J. Cuevas. Demodulation of a single interferogram by use of a two–dimensional regularized phase–tracking technique. *Applied Optics*, 36(19):4540–4548, 1 July 1997.

[57] M. Servin, R. Rodriguez-Vera, J. L. Marroquin, and D. Malacara. Phase–shifting interferometry using a two–dimensional regularized phase–tracking technique. *Journal of Modern Optics*, 45(9):1809–1819, 1998.

[58] Manuel Servin, Francisco Javier Cuevas, Daniel Malacara, Jose Luis Marroquin, and ramon Rodriguez-Vera. Phase unwrapping through demodulation by use of the regularized phase–tracking technique. *Applied Optics*, 38(10):1934–1941, 1 April 1999.

[59] Manuel Servin, Jose Luis Marroquin, Daniel Malacara, and Francisco Javier Cuevas. Phase unwrapping with a regularized phase–tracking system. *Applied Optics*, 37(10):1917–1923, 1 April 1998.

[60] Mikael Sjodahl and per Synnergren. Measurement of shape by using projected random patterns and temporal digital speckle photography. *Applied Optics*, 38(10):1990–1997, 1 April 1999.

[61] V. Srinivasan, H. C. Liu, and M. Halioua. Automated phase–measuring profiometry of 3–D diffuse objects. *Applied Optics*, 23(18):3105–3108, September 1984. Reprinted in *Selected Papers on Optical Moire and Applications*, SPIE Milestone Series, Guy Indebetouw and Robert Czarnek editors, SPIE Optical Engineering Press, Bellingham, Washington, 1992.

[62] V. Srinivasan, H. C. Liu, and Maurice Halioua. Automated phase–measuring profilometry: a phase mapping approach. *Applied Optics*, 24(2):185–188, January 1985.

[63] Paul Stephenson, David R. Burton, and Michael J. Lalor. Data validation techniques in a tiled phase unwraping algorithm. *Optical Engineering*, 33(11):3703–3708, November 1994.

[64] Glenn Stutz. Laser scanners extend machine–vision capability. *Laser Focus World*, 35(7):125–129, July 1999.

[65] Mitsuo Takeda, Quan Gu, Masaya Kinoshita, Hideaki Takai, and Yosuke Takahashi. Frequency–multiplex Fourier–transform profilometry: A single–shot three–dimensional shape measurement of objects with large height discontinuities and/or surface isolations. *Applied Optics*, 36(22):5347–5354, 1 August 1997.

[66] Mitsuo Takeda, Hideki Ina, and Seiji Kobayashi. Fourier–transform method of fringe–pattern analysis for computer–based topography and interferometry. *Journal of the Optical Society of America*, 72(1):156–160, January 1982. Reprinted in *Selected Papers on Optical Moire and Applications*, SPIE Milestone Series, Guy Indebetouw and Robert Czarnek editors, SPIE Optical Engineering Press, Bellingham, Washington, 1992.

[67] Mitsuo Takeda and Kazuhiro Mutoh. Fourier transform profilometry for the automatic measurement of 3–D object shapes. *Applied Optics*, 22(24):3977–3982, 15 December 1983.

[68] T. Tsuruta and Y. Itoh. Interferometric generation of counter lines on opaque objects. *Optics Communications*, 1(1):34–36, April 1969. Reprinted in *Selected Papers on Optical Moire and Applications*, SPIE Milestone Series, Guy Indebetouw and Robert Czarnek editors, SPIE Optical Engineering Press, Bellingham, Washington, 1992.

[69] Zhi G. Wang. Wavelength spectral compensation in fused fiber couplers. Master's thesis, Virginia Polytechnic Institute and State University, Blacksburg, Virginia, February 1996.

[70] R. Windecker and H. J. Tiziani. Topometry of technical and biological objects by fringe projection. *Applied Optics*, 34(19):3644–3650, 1 July 1995.

[71] Xinjun Xie, Michael J. Lalor, David R. Burton, and Michael M. Shaw. Phase–unwrapping algorithm in the presence of discontinuities using a system with crossed grating. *Optics and Lasers in Engineering*, 29(1):49–59, 1998.

[72] Toyohiko Yatagi. Intensity based analysis methods. In David W. Robinson and Graeme T. Reid, editors, *Interferogram Analysis, Digital Fringe Pattern Measurement Techniques*, chapter 4, pages 72–93. Institute of Physics Publishing, Bristol, 1993.

[73] Hong Zhao, Wenyi Chen, and Yashan Tan. Phase–unwrapping algorithm for the measurement of three–dimensional object shapes. *Applied Optics*, 33(20):4497–4500, 10 July 1994.

Vita

Timothy L. Pennington received his Bachelor's of Science in Electrical Engineering from the Virginia Military Institute in Lexington, Virginia, where he graduated as a Distinguished Graduate. Upon entering active duty status in the United Status Air Force, Lt. Pennington attended the Air Force Institute of Technology at Wright–Patterson AFB, Ohio, where he received a Master's Degree in Electrical Engineering. Lt. Pennington's thesis topic was a performance comparison of two wavefront sensors used in adaptive optics. After graduation, Lt. Pennington was assigned to the Starfire Optical Range, Air Force Phillips Laboratory at Kirtland AFB, New Mexico, as an adaptive optics systems engineer. In 1997, Captain Pennington was selected to enter a Ph.D. program at Virginia Polytechnic Institute and State University. Upon completion, Caption Pennington will be assigned to Kelly AFB, Texas.